

A young spectroscopic binary in a quintuple system part of the Local Association.

Carlos Cardona Guillén^{1,2}, Nicolas Lodieu^{1,2}, Víctor J. S. Béjar^{1,2}, David Baroch^{3,4}, David Montes⁵,
Matthew J. Hoskin^{6,7}, Sandra V. Jeffers⁸, Felipe Murgas^{1,2}, Pier-Emmanuel Tremblay⁶, Patrick Schöfer⁸,
Daniel Harbeck⁹, and Curtis McCully⁹

¹ Instituto de Astrofísica de Canarias, Vía Láctea s/n, E-38205 La Laguna, Tenerife, Spain

² Departamento de Astrofísica, Universidad de La Laguna, E-38200, La Laguna, Tenerife, Spain

³ Institut de Ciències de l'Espai (ICE, CSIC), Campus UAB, c/Can Magrans s/n, E-08193 Bellaterra, Barcelona, Spain

⁴ Institut d'Estudis Espacials de Catalunya (IEEC), c/ Gran Capità 2-4, E-08034 Barcelona, Spain

⁵ Departamento de Física de la Tierra y Astrofísica & IPARCOS-UCM (Instituto de Física de Partículas y del Cosmos de la UCM), Facultad de Ciencias Físicas, Universidad Complutense de Madrid, E-28040 Madrid, Spain

⁶ Department of Physics, University of Warwick, Coventry, CV4 7AL, UK

⁷ Centre for Exoplanets and Habitability, University of Warwick, Coventry, CV4 7AL, UK

⁸ Max-Planck-Institut für Sonnensystemforschung, Justus-von-Liebig-Weg 3, 37077 Göttingen, Germany

⁹ Las Cumbres Observatory Global Telescope Network, 6740 Cortona Dr. Suite 102, Goleta, CA 93117

September 6, 2021

ABSTRACT

Context. Double-lined spectroscopic (SB2) binaries allow us to obtain a direct determination of the masses of their components, which is essential to test stellar models. Although these objects only provide a lower limit for the mass, they are more abundant than their eclipsing counterparts as they are not as strongly limited by the inclination of their orbit.

Aims. Our aim is to derive the orbital and physical parameters of GJ 1284, a young SB2. We also revise the membership of this system and its two wide co-moving companions, GJ 898 and GJ 897AB, to a young moving group to assess, along with other youth indicators, their age. Afterwards, we compare the results from these analyses and the photometry of these systems with several pre-main-sequence evolutionary models.

Methods. We use high-resolution spectra to determine the radial velocity of each component of GJ 1284 and the orbit of the system alongside its systemic velocity. Additionally, we use TESS photometry to derive the rotational period of the GJ 1284 and its two wide companions.

Results. GJ 1284 is a binary system located at approximately 16 pc with an eccentric orbit ($e = 0.505$) of 11.83 d period made up of an M2–M2.5 + M3–M3.5 with minimum masses of $M \sin^3 i = 0.141 \pm 0.003$ and $0.1189 \pm 0.003 M_{\odot}$, respectively. The revised systemic velocity of $\gamma = 0.84 \pm 0.14 \text{ km s}^{-1}$ suggests that it is a member of the Local Association. The kinematics together with other activity and youth indicators imply an age of 110–800 Myr for this system and its two companions.

Conclusions. The isochronal ages derived from the comparison of the photometry with several evolutionary models are younger than the age estimated from the activity indicators for the three co-moving systems. The masses for the components of GJ 1284, derived from their luminosity and age using the different models, are not consistent with the masses derived from the photometry, except for the PARSEC models, but are compatible with dynamical masses of double-lined eclipsing binaries with similar ages and spectral types. The effect of magnetic activity in the form of spots can reconcile to some extent the photometric and dynamical masses, but is not considered in most of the evolutionary models.

Key words. binaries: spectroscopic – techniques: radial velocities – stars: evolution – stars: pre-main sequence – open clusters and associations: individual: Local Association

1. Introduction

The observational knowledge of fundamental properties of the stars is the basis for most of the astrophysics models explaining the evolution of stars and galaxies. In particular, the mass of the star is the main property that regulates its evolution and eventual fate. The determination of stellar masses with high precision is then essential to constrain these models. Double-lined eclipsing binaries (EBs) provide a unique opportunity to obtain direct measurements of the mass and radius of its stellar components with accuracies of $\sim 1\%$ (Torres et al. 2010). However, the number of systems where this precision has been achieved is relatively low (Torres et al. 2010; Southworth 2015). This

holds true, especially, for young (< 800 Myr) low-mass stars and brown dwarfs, as only a few are known and have accurate mass and radius determinations (David et al. 2019; Lodieu et al. 2020, and references therein). These systems are necessary to constrain pre-main-sequence (PMS) evolutionary models. Most of them have been recently discovered, made possible by the advent of ground-based surveys such as SuperWASP (Pollacco et al. 2006), and space missions such as CoRoT (Baglin et al. 2006), Kepler (Koch et al. 2004; Borucki et al. 2007), or TESS (Ricker et al. 2014), which monitor almost the whole night sky.

The detection of EBs is heavily constrained by the inclination of the orbit of the system (i.e. only nearly edge-on configurations produce eclipses). On the other hand, orbital config-

urations of double-lined spectroscopic binaries (SB2) are not as strongly limited. Thus, the number of known young SB2s (e.g. Dudorov & Eretnova 2016; Shkolnik et al. 2017; Zúñiga-Fernández et al. 2021, and references therein) is higher than EBs. Most of these young SB2s were discovered, also serendipitously, as part of spectroscopic surveys focusing on relatively few members of young stellar associations, the majority of them solar-type (FGK) stars, while the number of M dwarfs still remains low. Moreover, their orbits, for the most part, have not been characterised to date as only a few spectra for each of them are available. However, SB2s do not provide any information about the radii of the system components and only a minimum limit for their masses, even though they are more abundant than EBs.

The determination of the age of the system is a step needed to test the validity of the predictions of PMS models. This is usually achieved comparing the photometry of the object against isochrones derived from evolutionary models (e.g. Malo et al. 2014b; Herczeg & Hillenbrand 2015; Bell et al. 2015). In open clusters and young moving groups (YMGs), we can assume that all the members were born roughly at the same time (Zuckerman & Song 2004). Under this assumption we can expect that the age derived from the isochrones should be consistent for all of them. This provides a powerful tool for determining the age of a particular open cluster or YMG, and subsequently of any of its newly identified members. For this reason, a proper characterisation of the evolutionary models is also important for determining stellar ages. Nonetheless, the age of the members of open clusters and YMGs can also be estimated using other methods that are mostly independent or do not rely so heavily on evolutionary models, for example traceback simulations to find the convergence point; lithium depletion boundary (LDB) determinations; or age relations with youth indicators such as rotational period, X-ray, or $H\alpha$ emission (see Soderblom 2010, and references therein)

The relative proximity to the Sun of most YMG members means they are bright enough to achieve a radial velocity (RV) precision of km s^{-1} with small telescopes (~ 1 m) needed to measure dynamical masses. As part of an observing campaign with the Mercator 1.2 m telescope, we observed several early- to mid-type M dwarfs previously classified as members of YMGs in the literature. We confirmed one of these targets, GJ 1284, as an SB2 previously identified by Gizis et al. (2002). Later on, we also characterised the orbit of this system using the Mercator spectra and data from other facilities obtained during this and subsequent campaigns, and data gathered from the literature. The system was initially classified as a member of either the Beta Pictoris Moving Group (β PMG; Barrado y Navascués et al. 1999; Zuckerman et al. 2001) or the Columba Association (COL; Torres et al. 2008) by Malo et al. (2013). Moreover, one other system, GJ 898, had been identified kinematically as a wide co-moving companion to GJ 1284 (Shaya & Olling 2011). This wide companion forms part of a triple system alongside another binary star, GJ 897AB (Kuiper 1943). The three objects combined form a wide quintuple system. In this work we revise the membership of GJ 1284 to a YMG based on its new kinematics and youth indicators, which suggests that it belongs to the Local Association (LA; Eggen 1975; Montes et al. 2001), the same YMG as GJ 898 and GJ 897 (Montes et al. 2001; Makarov et al. 2008).

The LA, also commonly known as the Pleiades moving group, is one of the first classical YMGs identified by Eggen (1975) who initially described it as a stream associated with the Pleiades open cluster. Later on, Asiain et al. (1999) and López-

Santiago et al. (2006) revealed that LA is actually made up of several subgroups with ages ranging from 10–300 Myr.

In this work we characterise the orbit GJ 1284 using spectra collected with four different high-resolution spectrographs, and compare the results against the predictions made by several stellar evolution models. In Sect. 2 we introduce the GJ 1284 system and review the literature about this object and its wide companions. In Sect. 3 we describe the high-resolution spectra collected over several observing campaigns complemented by additional photometric and spectroscopic datasets from the literature. In Sect. 4 we measure the RVs from the spectra and determine the orbital parameters of the system. We also infer the rotational period of GJ 1284 system and its wide companions. Finally, in Sect. 5 we propose an age range for the three systems and compare their photometry and the mass of the GJ 1284 components against PMS evolutionary models and similar studies.

2. GJ 1284

2.1. Description of the system

GJ 1284 is located at a distance $d = 15.906 \pm 0.019$ pc (*Gaia* early Data Release 3, eDR3; Prusti et al. 2016; Brown et al. 2020). It has been extensively analysed as a member of the solar neighbourhood due to its proximity, and has been part of several direct-image searches for substellar companions (e.g. Galicher et al. 2016; Meshkat et al. 2017; Naud et al. 2017; Nielsen et al. 2019). The system was classified as an M3.0V star by Hawley et al. (1996). More recently, Torres et al. (2006) classified it as an M2.0Ve with an uncertainty of one subclass using high-resolution spectra. In this work we estimate the spectral types of the binary components based on the colours derived from the photometric magnitudes.

Gizis et al. (2002) measured short-term variations in the RVs of GJ 1284 of over 46 km s^{-1} and identified it as an SB2, even though they did not characterise its orbit. Later it was again identified as an SB2 by Torres et al. (2006), who obtained three more RV measurements with a mean value of -5.7 km s^{-1} . Jeffers et al. (2018) also measured the RV of GJ 1284 on seven consecutive nights obtaining a mean value of -4.4 km s^{-1} with a peak-to-peak variation of 62.63 km s^{-1} . Additionally, Schneider et al. (2019) measured a single value of $8.18 \pm 1.07 \text{ km s}^{-1}$. Finally, Sperauskas et al. (2019) obtained two more values of -0.4 ± 1.0 and $-14.6 \pm 1.0 \text{ km s}^{-1}$. A summary of all the individual measurements is given in Table 1. Nonetheless, the orbital parameters of this binary system have not been derived due to the lack of continuous monitoring.

Torres et al. (2006) first identified GJ 1284 as a young object (< 600 Myr) based on several youth indicators. Malo et al. (2013) proposed it as a member of either COL (99.2%) or β PMG (99.9%), depending on whether or not they included the mean RV value from Torres et al. (2006) in the analysis. Following this work, GJ 1284 has been commonly catalogued as a either a member of COL (Malo et al. 2014a; Bell et al. 2015; Naud et al. 2017) or β PMG (Elliott et al. 2016; Shkolnik et al. 2017). More recently, it has been rejected as a member of these two YMGs (Gagné et al. 2018; Schneider et al. 2019) and was classified as a field star (Janson et al. 2017) using the updated astrometry from *Gaia*. Nevertheless, the analysis of the membership of this object in a YMG is based on the average value of the available RV measurements, not on its systemic velocity.

Malo et al. (2014a) compiled the value of several youth indicators for members of YMGs, including GJ 1284. In particular, four youth indicators were considered: the projected ro-

Table 1. Compilation of RVs measured for GJ 1284 from the literature.

RV [km s ⁻¹]	Ref
+11.7 ± 1.5 ^a	Giz2002
-4.7 ± 1.5 ^a	Giz2002
-16.7 ± 1.5 ^a	Giz2002
+30.1 ± 1.5 ^a	Giz2002
-5.7 ^b	Tor2006
+43.74 ± 0.11	Jef2018
+5.74 ± 0.15	Jef2018
-16.08 ± 0.22	Jef2018
-18.89 ± 0.12	Jef2018
-17.14 ± 0.35	Jef2018
-15.89 ± 0.10	Jef2018
-12.56 ± 0.10	Jef2018
8.18 ± 1.07	Sch2019
-0.4 ± 1.0	Spe2019
-14.6 ± 1.0	Spe2019

References. Giz2002: Gizis et al. (2002); Tor2006: Torres et al. (2006); Jef2018: Jeffers et al. (2018); Sch2019: Schneider et al. (2019); Spe2019: Sperauskas et al. (2019);

Notes. ^(a) The associated error corresponds to the internal consistency mentioned in that work. ^(a) Mean value calculated from three different epochs. No uncertainty is provided.

tational velocity ($v \sin i$), the pseudo-equivalent width (pEW) of the H α emission line, the X-ray flux, and the pEW of the lithium 6707.8 Å absorption line. They report a value of $v \sin i = 3.9 \pm 1.2 \text{ km s}^{-1}$, in agreement with Torres et al. (2006). However, the authors note that this value might not be reliable because of the binarity of the system. A value of $\text{pEW}(\text{H}\alpha) = -3.3 \text{ \AA}$ was obtained by Riaz et al. (2006) from medium-resolution spectra taken at the Cerro Tololo Inter-American Observatory (CTIO) 1.5 m telescope. Again, this value could be affected by the binarity, although it also agrees with the $\text{pEW}(\text{H}\alpha) = -3.23 \pm 0.08 \text{ \AA}$ obtained by Jeffers et al. (2018) from high-resolution spectra. The $\log f_{\text{X}} = -11.44 \text{ erg s}^{-1} \text{ cm}^{-2}$ also comes from Riaz et al. (2006) using ROSAT data (Voges et al. 1999) and the conversion relations described in Schmitt et al. (1995). Finally, Torres et al. (2006) report that the Li 6708 Å line was not detected in their spectra.

2.2. Wide companions

Two other stellar systems are identified in the literature as common proper motion companions to GJ 1284: GJ 898 (Shaya & Olling 2011) and GJ 897AB (Kuiper 1943). We describe these two systems below.

GJ 898 is a K6 (Torres et al. 2006) located at a distance of $d = 14.549 \pm 0.006 \text{ pc}$ and classified as a member of the Local Association by Montes et al. (2001) according to its kinematics. The projected separation in the sky to GJ 1284 is 3.59 deg or $\sim 2 \times 10^6 \text{ au}$ (roughly 1 pc) at their mean distance. The physical separation of 1.66 pc together with a difference in their proper motions of over 10σ (*Gaia* eDR3; Table 2) may suggest this is a chance alignment. Nonetheless, the galactocentric UVW velocities for GJ 898 and GJ 1284 (Sect. 5.1) are in very good agreement (Table 2; Fig. 1). The difference in the astrometry can thus be explained as a projection effect consequence of their wide

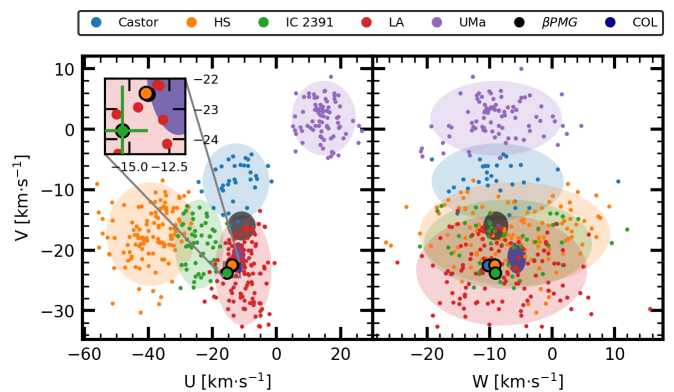


Fig. 1. Revised galactocentric UVW velocities of GJ 1284 (blue), GJ 898 (orange), and GJ 897AB (green) from this work compared to other YMG members from Montes et al. (2001). The ellipses represent the 2σ values of UVW for each YMG. Similarly, we overplot β PMG and COL as defined by Gagné et al. (2018).

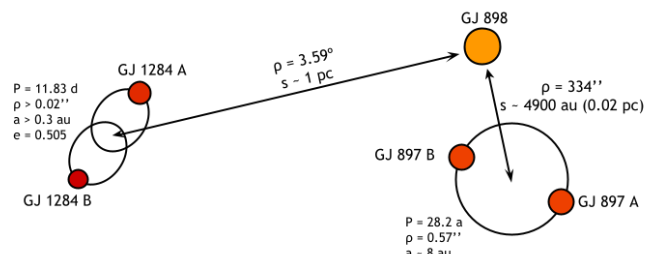


Fig. 2. Schematic view of the spatial configuration of the quintuple system made up of GJ 898, GJ 1284AB, and GJ 897AB. Sizes and distances are not to scale.

separation. In Sect. 5.2 we analyse whether the two systems are physically bound.

GJ 897AB was identified as a companion to GJ 898 by Kuiper (1943), and therefore is also a companion to GJ 1284. It is a resolved tight visual binary ($\rho = 0.57''$; Mason et al. 2002) formed by two components of similar magnitude ($V_A = 11.14 \text{ mag}$; $V_B = 11.17 \text{ mag}$; WDS) and mass ($0.5 \pm 0.1 M_{\odot}$; Heintz 1986a), which suggests a similar spectral type M2–M3 (Riaz et al. 2006; Torres et al. 2006). The orbit of the system is nearly edge-on ($i = 89.30^{\circ}$) with a period of 28.2 years (Heintz 1986b). While Woolley et al. (1970) list a distance for GJ 897 of $14.5 \pm 2.7 \text{ pc}$ and Gliese & Jahreiss (1991) give $12.9 \pm 9.9 \text{ pc}$, the separation of the components combined with the inclination of the orbit affects the quality of the astrometric solutions of more modern catalogues. For instance, Hipparcos lists a parallax of $5 \pm 34 \text{ mas}$ (van Leeuwen 2007), while *Gaia* does not provide a full astrometric solution in the last eDR3. In Table 2 we list the parallax and proper motions from the dynamical solution provided by Tokovinin (2018) for GJ 897AB, which are in closest agreement with the values for GJ 898. In this work we adopt for GJ 897AB the distance and proper motions of GJ 898 given their higher precision and the proximity of the two objects in the sky, which indicates they are most probably physical companions located at the same distance. Makarov et al. (2008) also noted that the space velocities of GJ 897AB and GJ 898 match those of the LA members from Montes et al. (2001), and supported this assessment with other activity indicators (see Sect. 5.1).

We performed a search for other common proper motion systems in a radius of up to 10 degrees using the *Gaia* eDR3 data,

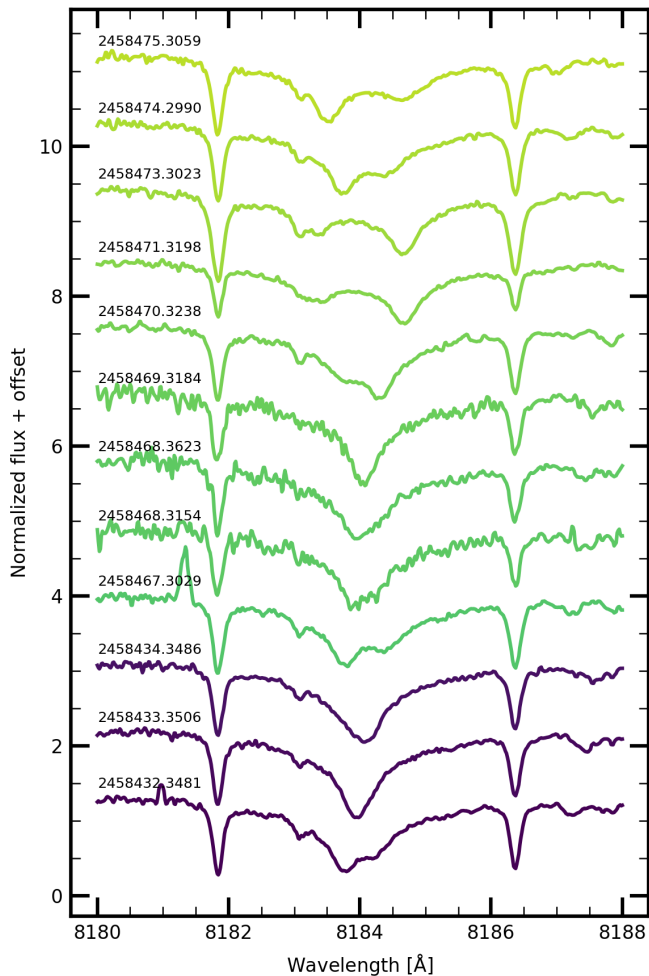


Fig. 3. HERMES spectra of GJ 1284 showing the Na I λ 8183.25 Å line.

but it did not produce any additional candidates. All together, GJ 898, GJ 897AB, and GJ 1284 form a group of at least five stellar objects with very similar galactocentric velocities, with GJ 898 being the most massive component. A schematic of the configuration of this quintuple system is shown in Fig. 2. The existence of this common proper motion system has an implication on the determination of the age of GJ 1284. As previously mentioned, both GJ 898 and GJ 897AB have been associated with LA in the literature. In Sect. 5.1 we discuss the membership of the three systems in a YMG based on their kinematics and other youth indicators to infer an age for the quintuplet.

3. Observations

We gathered 27 spectra for GJ 1284 with four distinct high-resolution spectrographs (Table 3). Additionally, this object and the two wide companions described in the previous section were observed by TESS, although the individual components of GJ 1284 and GJ 897AB are not resolved in the images.

3.1. Spectroscopy

3.1.1. HERMES

We first observed and identified GJ 1284 as an SB2 with the High Efficiency and Resolution Mercator Echelle Spec-

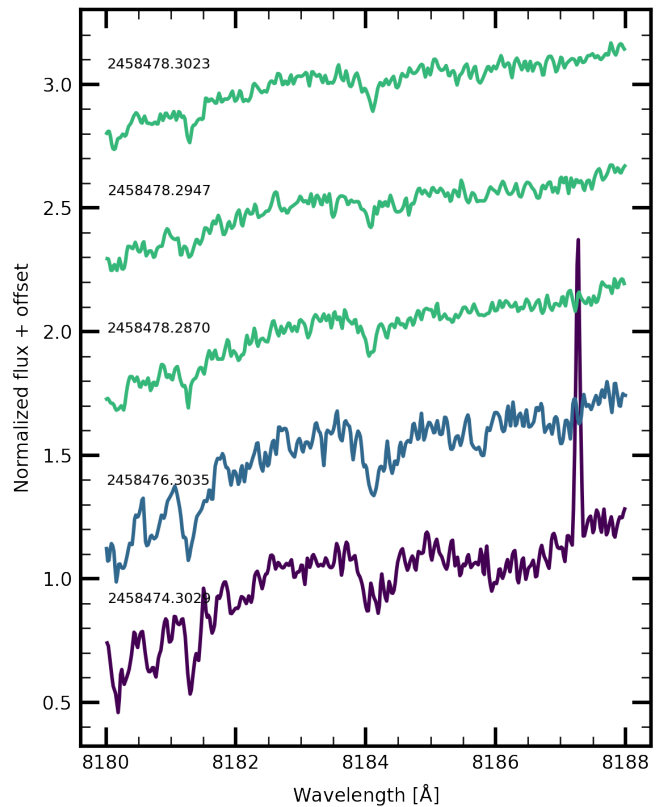


Fig. 4. NRES spectra of GJ 1284 centred around the Na I λ 8183.25 Å line.

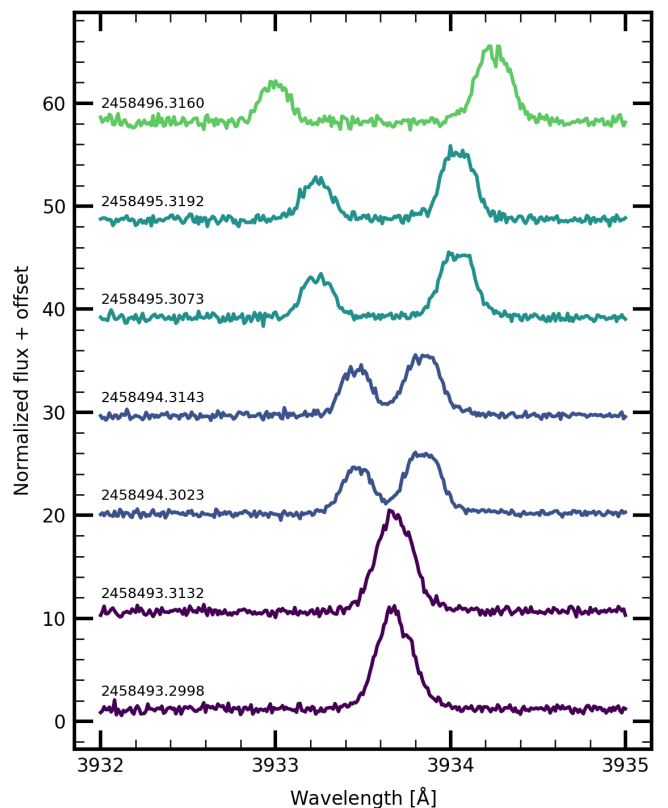


Fig. 5. HARPS-N spectra of GJ 1284 focused on the Ca II-H λ 3968.47 Å line.

Table 2. Stellar parameters of the GJ1284 system and its two wide companions.

Parameter	Value				References ^a
<i>Name and identifiers</i>					
Main identifier	G 273-59	HD 221503	BD-17 6768		
GI	1284	898	897A	897B	
TIC	9212046	434103018	434103039		
<i>Coordinates and kinematics</i>					
α (J2000)	23:30:13.44	23:32:49.40	23:32:46.98	23:32:46.98	2
δ (J2000)	-20:23:27.46	-16:50:44.32	-16:45:12.34	-16:45:11.74	2
π [mas]	62.67 ± 0.09	68.70 ± 0.06	64.8 ± 4.1^b		2, 2, 3
d [pc]	15.906 ± 0.019	14.549 ± 0.006	15.15 ± 0.46		2, 2, 3
$\mu_\alpha \cos \delta$ [mas a ⁻¹]	313.50 ± 0.15	340.98 ± 0.12	352.0 ± 2.6		2, 2, 3
μ_δ [mas a ⁻¹]	-205.41 ± 0.15	-218.98 ± 0.07	-216.1 ± 2.7		2, 2, 3
V_r [km s ⁻¹]	0.84 ± 0.14	-0.845 ± 0.0012	-1.6 ± 1.7		1, 2, 4
U [km s ⁻¹]	-13.837 ± 0.026	-13.942 ± 0.009	-15.4 ± 0.8		1
V [km s ⁻¹]	-22.499 ± 0.021	-22.471 ± 0.007	-23.7 ± 0.7		1
W [km s ⁻¹]	-10.231 ± 0.015	-9.184 ± 0.003	-9.1 ± 1.6		1
<i>Spectral type and photometry</i>					
SpT	M2–M2.5V + M3–M3.5V	K6.0V	M2.5V		1, 4, 5
B [mag]	12.59 ± 0.03	9.890 ± 0.019	11.79 ± 0.03		6, 7, 6
V [mag]	11.11 ± 0.03	8.600 ± 0.013	10.34 ± 0.04		6, 7, 6
G [mag]	9.9210 ± 0.0020	8.0816 ± 0.0008	10.033 ± 0.005	10.058 ± 0.004	2
BP [mag]	11.319 ± 0.003	8.829 ± 0.004	10.548 ± 0.008	10.556 ± 0.007	2
RP [mag]	8.777 ± 0.004	7.251 ± 0.004	8.198 ± 0.005	8.210 ± 0.009	2
J [mag]	7.200 ± 0.019	6.236 ± 0.019	6.71 ± 0.20		8
H [mag]	6.61 ± 0.04	5.61 ± 0.03	6.08 ± 0.03		8
K [mag]	6.329 ± 0.026	5.473 ± 0.016	5.858 ± 0.016		8
g [mag]	12.4084 ± 0.0010	10.86 ± 0.05	9.70 ± 0.04		9
r [mag]	10.50 ± 0.01	8.308 ± 0.011	9.91 ± 0.11		9
i [mag]	10.88 ± 0.05	9.72 ± 0.08	8.765 ± 0.021		9
NUV [mag]	18.02 ± 0.04	16.900 ± 0.015	17.253 ± 0.017		10, 11, 10
<i>Additional information</i>					
$v \sin i$ [km s ⁻¹]	3.9 ± 1.2	7.47 ± 1.00	7.1 ± 1.2		12, 13, 4
pEW(H α) [Å]	-3.23 ± 0.08	0.12 ± 0.04	-1.051		12, 13, 14
$\log L_X$ [erg s ⁻¹] ^c	29.04 ± 0.04	28.15 ± 0.11	29.22 ± 0.044		15
P_{rot} [d]	7.45 ± 0.1	11.5 ± 0.1	5.00 ± 0.02		1

References. (1) This work; (2) *Gaia* eDR3: Prusti et al. (2016); Brown et al. (2020); (3) Tokovinin (2018); (4) Torres et al. (2006); (5) Riaz et al. (2006); (6) APASS: Henden et al. (2016); (7) SKY2000: Myers et al. (2015); (8) 2MASS: Skrutskie et al. (2006); (9) UCAC4: Zacharias et al. (2013); (10) Schneider et al. (2019); (11) Riedel et al. (2017); (12) Jeffers et al. (2018); (13) López-Santiago et al. (2010); (14) Jones & West (2016); (15) ROSAT: Voges et al. (1999).

Notes. ^(a) Reference numbers for the three systems are separated by commas; a single number is provided whenever it is the same for all of them. ^(b) For the purposes of this work we adopt the parallax value from GJ 898 given the high uncertainty on the parallax determination of GJ 897 and their proximity and shared kinematics. ^(c) Calculated using the relations from Riaz et al. (2006).

trograph (HERMES; Raskin et al. 2011) as part of observing programme CAT-141-MULTIPLE-2/18B (PI: Cardona Guillén). We also obtained additional spectra with this same instrument through programmes 128-Mercator4/18B (PI: Montes) and ITP18_8 (PI: Tremblay). HERMES is a fibre-fed echelle spectrograph mounted on the Mercator 1.2 m semi-robotic telescope located in the Roque de los Muchachos Observatory (ORM) on La Palma, Spain. A total of 11 spectra were gathered over several runs spanning from 9 November to 22 December 2018 under clear conditions and a seeing of ~ 0.8 arcsec. The spectra were taken using the high-resolution mode (HRF) with an exposure time of 1 800 s. This mode provides a spectral resolution $R \sim 85 000$ and a wavelength coverage from 377 to 900 nm through a 2.5 arcsec fibre equipped with an image

slicer. The data were reduced by the automated pipeline and RV toolkit (HermesDRS¹). This tool provides one-dimensional wavelength-calibrated spectra using the standard reduction procedure (bias subtraction, flat-field correction, order extraction, and wavelength calibration) from which we derive the RV measurements described in Sect. 4.1. Figure 3 shows the HERMES spectra for each epoch zoomed in around the Na I $\lambda 8183.25$ Å.

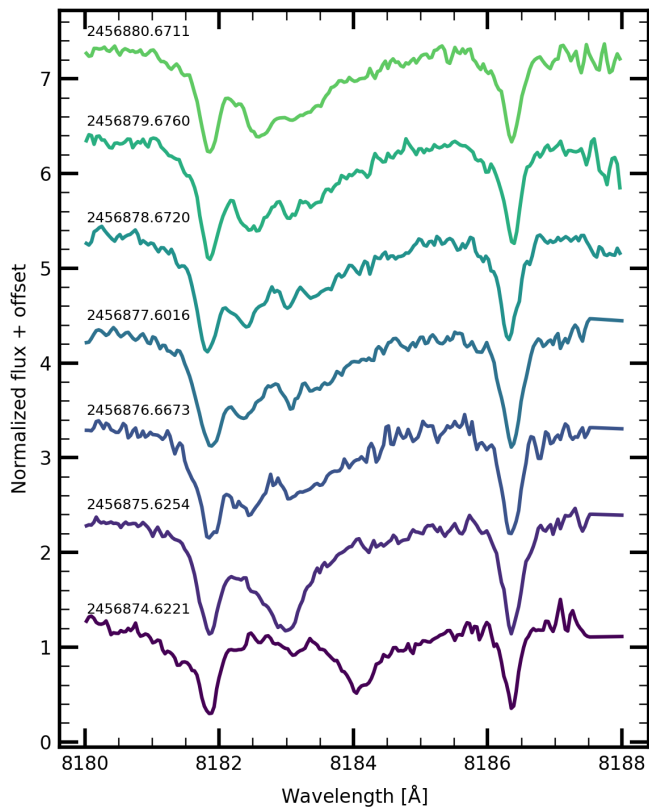
3.1.2. NRES

We obtained five additional spectra on three separate nights (21, 23, and 25 December 2018) using the Network of Robotic

¹ <http://www.mercator.iac.es/instruments/hermes/drs/>

Table 3. Instrumental configuration of the spectrographs used in this paper.

Instrument	Telescope	R	No. orders	$\Delta\lambda$ [nm]	No. epochs	Δt [d]	t_{exp} [s]	Configuration
HERMES	Mercator	85 000	54	377–900	11	43	1 800	HRF
CAFE	Calar Alto 2.2m	62 000	84	396–950	7	7	1 800	
HARPS-N	Telescopio Nazionale Galileo	115 000	69	383–690	4	4	900	GIARPS
NRES	LCOGT 1-metre telescopes	53 000	67	380–870	5	4	1 800	

**Fig. 6.** CAFE spectra of GJ 1284 depicting the Na I λ 8183.25 Å line.

Echelle Spectrographs (NRES; Siverd et al. 2018) as part of programme KEY2017AB-002a (PI: Brown). NRES is a set of identical high-resolution spectrographs mounted on the 1 m telescopes of the Las Cumbres Observatory network (LCOGT; Brown et al. 2013). Each spectrograph is fibre-fed by two telescopes simultaneously, and has a resolution $R \sim 53\,000$ and a wavelength coverage from 380 to 860 nm. The spectra used in this work were obtained using the node located in the South African Astronomical Observatory (SAAO) in Sutherland, South Africa. Currently, three other NRES elements are available in the LCOGT nodes located in Chile, the United States, and Israel. The data were reduced using the automatic NRES pipeline². The pipeline yields a one-dimensional spectrum calibrated in wavelength similarly to HERMES. In Fig. 4 we plot the NRES spectra for each epoch showing the Na I λ 8183.25 Å.

² <https://lco.global/documentation/data/nres-pipeline/>

3.1.3. HARPS-N

We also observed the target using the High Accuracy Radial velocity Planet Searcher North (HARPS-N; Cosentino et al. 2012) on four consecutive nights between 9 and 12 January 2019 under programme CAT-141-MULTIPLE-2/18B (PI: Cardona Guillén). HARPS-N is an echelle spectrograph mounted on the 3.58 m Telescopio Nazionale Galileo (TNG) also located in the ORM. The design of the instrument is similar to its predecessor HARPS (Mayor et al. 2003), covering a wavelength range from 383 to 690 nm with a resolution of $R \sim 115\,000$. We obtained two spectra with exposure times of 900 s on each of the observing nights, except on 12 January 2019 when we obtained only one spectrum. These spectra were reduced automatically at the end of each night using the standard HARPS-N data reduction pipeline (Cosentino et al. 2014; Smareglia et al. 2014). Figure 5 shows the HARPS-N spectra around the Ca II-H λ 3968.47 Å line.

3.1.4. CAFE

We also used spectra collected by Jeffers et al. (2018) with the Calar Alto Fiber-fed Echelle spectrograph (CAFE; Aceituno et al. 2013). CAFE is a fibre-fed echelle spectrograph mounted on the Calar Alto 2.2 m telescope in Centro Astronómico Hispano Alemán (CAHA) in Almería, Spain. The spectrograph has a wavelength coverage ranging from 396 to 950 nm spanning 84 orders with a resolution $R \sim 62\,000$. A total of seven spectra were taken over the same number of consecutive nights from 5 August to 11 August 2014 with exposure times of 1 800 s. The data were reduced using a version of the REDUCE package (Piskunov & Valenti 2002). More details about the observations and the data reduction process can be found in Jeffers et al. (2018). Figure 6 shows the CAFE spectra at each epoch around the Na I λ 8183.25 Å.

3.2. Photometry

The Transiting Exoplanet Survey Satellite (TESS; Ricker et al. 2014) is a space mission launched on 18 April 2018. During its two-year prime mission, which started on 25 July 2018, TESS monitored more than 200 000 main-sequence stars, covering almost all of the sky using its four cameras with a combined field of view of $24^\circ \times 96^\circ$ in continuous campaigns of 27 days. A pre-selection of targets were monitored with a two-minute cadence.

GJ 1284 and its two co-moving companions GJ 898 and GJ 897AB were observed by TESS as part of Sector 2, from 22 August to 20 September 2018, and Sector 29, from 26 August to 22 September 2020. For GJ 1284 and GJ 897AB there is a two-minute cadence light curve available for each of these sectors, while for GJ 898 only the light curve for Sector 29 can be retrieved. The target input catalogue (TIC) numbers for the three objects are shown in Table 2; their light curves are publicly

available and can be downloaded from the Mikulski Archive for Space Telescopes (MAST) Portal³. The two-minute-cadence photometry includes two different sets of data: the single aperture photometry (SAP) light curve, and the pre-search data conditioning (PDC) light curve. The PDC light curve attempts to correct the common instrumental effects present in the SAP light curve. In this work we use the SAP light curve to avoid corrections that may affect the activity-induced photometric variations, especially in relatively slow rotators with low-amplitude variability like ours. The two-minute cadence light curves of the three systems are shown in Fig. 7.

4. Data analysis

4.1. Radial velocities determination

The usual approach to calculating the RV of an object with the cross-correlation function (CCF) technique can lead to the determination of less precise values in SBs because of the blending of the spectral lines of the binary components. For this reason we used TODMOR (Zucker et al. 2004) to derive the RV values from all the spectra gathered for this object. TODMOR is a multi-order implementation of the Two-Dimensional CORrelation technique (TODCOR; Zucker & Mazeh 1994). It uses a combination of two template spectra to simultaneously calculate the CCF for both components of the binary system. This technique is applied to each echelle order, combining the resulting CCFs into a single one to derive the RV.

We used a set of template spectra created using PHOENIX stellar models (Husser et al. 2013) as a reference to calculate the CCF. These templates have varying values of effective temperature (T_{eff}) that can be broadened to match the projected rotational velocity ($v \sin i$) of the star. We fixed the value for the metallicity $[\text{Fe}/\text{H}] = 0$ given the proximity of the system to the Sun. We used a range for T_{eff} from 3000 to 4000 K in steps of 100 K and for $v \sin i$ from 0 to 10 km s^{-1} in steps of 1 km s^{-1} . An additional parameter α was included to account for the flux-ratio between the two template spectra to calculate the CCF. We calculated the values that provide the best fit of the CCF using the HERMES spectrum observed closer to quadrature, when the lines of the binary components are most separated. We found that the optimal parameter values for the stellar templates are $T_{\text{eff}} = 3800 \pm 100$ K and $v \sin i = 6 \pm 1$ km s^{-1} for the primary component and $T_{\text{eff}} = 3600 \pm 100$ K and $v \sin i = 8 \pm 1$ km s^{-1} for the secondary, with a flux ratio $\alpha = 0.47 \pm 0.10$. These templates are used to derive the RV for the two components simultaneously at each epoch (see Zucker & Mazeh 1994, for more details). Taking advantage of the CCF per spectral order provided by TODMOR, we also inspected and excluded from the analysis those orders that are heavily contaminated by telluric lines, and those with low signal-to-noise ratios (S/N), mainly in the blue part of the spectrum where the peaks of the two components are not apparent in the CCF. The final RVs derived by TODMOR are given in Table 4.

In addition, we calculated and applied the barycentric correction (BVCOR) to each RV epoch. HARPS-N applies this correction to the spectra themselves so that the extracted RV values are already in the barycentric reference frame. Moreover, it also provides the Barycentric Julian Day (BJD). For HERMES the value for the BVCOR and the BJD of each exposure is calculated as part of the pipeline and provided in the header of each

image. Instead, CAFE and NRES do not provide these values as part of the automatic pipeline. For these instruments, we calculated the BJD and BVCOR at each epoch with the routines included in the *astropy* Python package⁴. This package uses an implementation of the expressions in Wright & Eastman (2014).

To improve the determination of the RVs we also accounted for relative drift in the wavelength calibration of the different instruments. To palliate this issue we tracked the position of the telluric lines at each epoch using the IRAF routine *fxcor* (Tody 1986) to calculate a one-dimensional CCF. We correlated the HERMES spectrum with the highest S/N, which provides the widest wavelength coverage of all the spectrographs, against the rest of the spectra and chose the regions where the presence of the telluric lines is more apparent (e.g. 8119–8179, 8203–8324, 8928–8997 Å). The drift of the telluric lines relative to the reference spectrum is calculated from the highest peak of the resulting CCF. For the HERMES spectra we find that the internal drift is comparable (< 0.5 km s^{-1}) to the uncertainty associated with the individual RV calculated using TODMOR. In the case of the CAFE spectra the internal drift is of the same order as HERMES, but there is a drift of ~ 1 km s^{-1} between the two instruments. For NRES the internal drift appears to be about ~ 0.5 km s^{-1} , similar to HERMES and also comparable to the systematic drift between the two instruments. Lastly, the internal drift in the HARPS-N spectra is lower than the precision we can achieve with this method of 0.1 km s^{-1} (i.e. there is no noticeable internal drift). Meanwhile, there seems to be a systematic drift of ~ -0.3 km s^{-1} with respect to the reference HERMES spectrum, lower than the internal drift of this spectrograph. For the final analysis, we corrected the RV values derived with TODMOR from the drifts measured using the telluric lines at each epoch (Table 4). The internal drifts show that the stability of the four spectrographs is good enough to characterise our binary system, which presents variations of over 60 km s^{-1} .

Table 4 includes the final RVs used in the orbital parameter determination (Sect. 4.2) and their uncertainties together with the BJD, barycentric, and telluric correction at each epoch. In Fig. 8 we plot the RVs as a function of time (top panel) and orbital phase (bottom panel).

4.2. Orbital parameters determination

We use the IDL code *rvfit* to determine the orbital parameters of the binary system (Iglesias-Marzoa 2015). This routine uses an adaptive simulated annealing global minimisation method to fit the two components of the system simultaneously with a Keplerian orbit defined by seven parameters: the orbital period (P), the time periastron (T_p), the eccentricity (e), the argument of periastron (ω), the RV amplitude of the two components ($K1$ and $K2$), and the systemic radial velocity (γ). From these we can derive lower bounds for the masses and semi-major axes of the binary components as well as the mass ratio $q = (M_1/M_2)$. We estimate an initial value for the orbital period from the phase-folded RV values. The excellent phase coverage of the orbit and the wide time span relative to the orbital period between the CAFE observations and the rest of the exposures allowed us to obtain a very precise initial value, close to the final value provided later on by *rvfit*. The priors and final parameters of the best solution (Fig. 8) to the simultaneous fit of the two components are shown in Table 5.

From this analysis, we determine a value for the systemic RV of GJ 1284 $\gamma = 0.84 \pm 0.14$ km s^{-1} . This value differs from

³ <https://mast.stsci.edu/portal/Mashup/Clients/Mast/Portal.html>

⁴ <https://docs.astropy.org/en/stable/index.html>

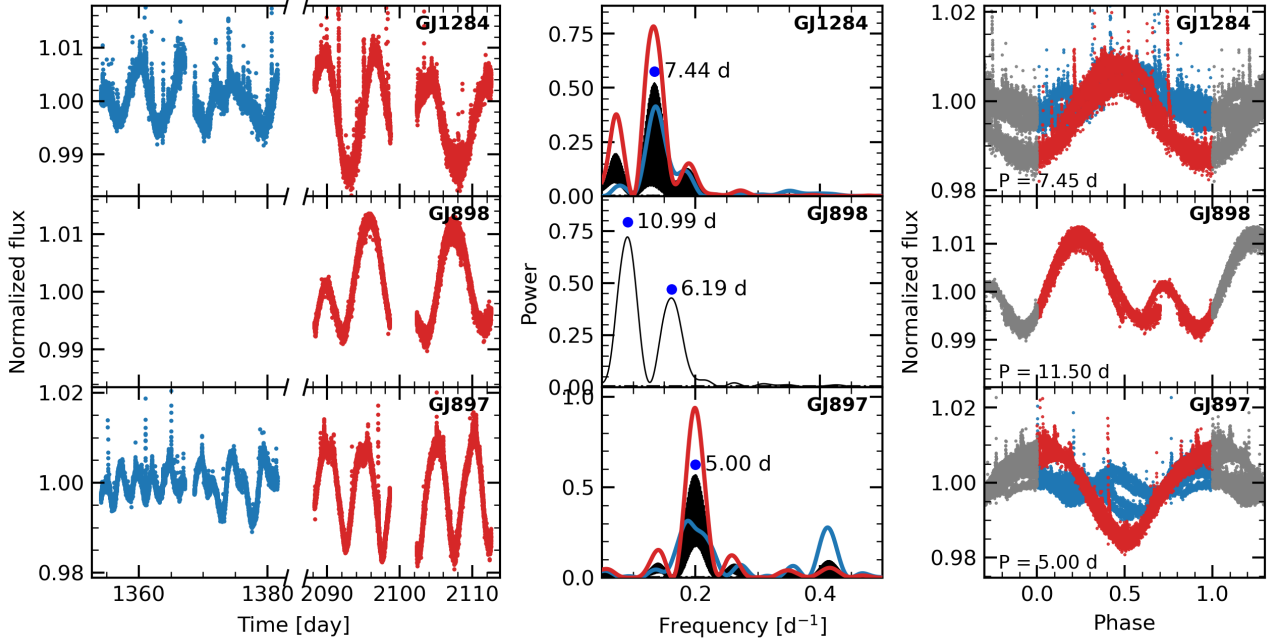


Fig. 7. TESS light curves and periodograms of GJ 1284 (top), GJ 898 (middle) and GJ 897 (bottom). *Left:* TESS photometric time series. *Middle:* GLS periodogram of the photometric time series. *Right:* Light curve phase-folded with the selected rotation periods in Table 2. We adjust the ordinate axis range to crop the stellar flares to better visualise the variations in the light curve due to the stellar rotation. The colours in all the panels correspond to data from Sector 2 (blue) or Sector 29 (red) or both combined (black).

Table 4. Summary of the RV measurements and the associated uncertainties obtained from the spectra along the BJD and barycentric corrections at each epoch.

BJD [d]	BVCOR [km s ⁻¹]	RV _{tell} [km s ⁻¹]	RV ₁ [km s ⁻¹]	σ _{RV1} [km s ⁻¹]	RV ₂ [km s ⁻¹]	σ _{RV2} [km s ⁻¹]	Inst
2456874.6254	14.97	1.24	44.65	0.20	-50.47	0.21	CAFE
2456875.6288	14.55	1.44	5.36	0.18	-3.67	0.19	CAFE
2456876.6708	14.03	1.44	-15.17	0.23	19.70	0.22	CAFE
2456877.6051	13.77	1.55	-18.48	0.22	24.14	0.22	CAFE
2456878.6756	13.17	1.99	-17.04	0.43	23.56	0.52	CAFE
2456879.6797	12.74	1.22	-14.85	0.49	19.62	0.49	CAFE
2456880.6748	12.32	1.22	-11.36	0.47	15.78	0.54	CAFE
2458432.3611	-25.72	-0.04	-7.67	0.09	9.75	0.14	HERMES
2458433.3635	-25.97	-0.74	-0.33	0.16	HERMES
2458434.3614	-26.19	0.00	5.45	0.10	-4.97	0.12	HERMES
2458467.3126	-28.90	-0.13	-10.16	0.09	13.27	0.13	HERMES
2458468.3350	-28.96	-0.31	-4.58	0.10	6.76	0.14	HERMES
2458468.3719	-28.96	-0.31	-4.58	0.10	6.76	0.13	HERMES
2458469.3278	-28.79	-0.30	1.01	0.16	HERMES
2458470.3332	-28.71	-0.14	10.21	0.09	-10.52	0.14	HERMES
2458471.3291	-28.61	0.01	23.17	0.08	-26.19	0.13	HERMES
2458473.3114	-28.36	-0.43	23.47	0.09	-25.48	0.14	HERMES
2458474.3081	-28.23	-0.11	-10.97	0.09	14.33	0.13	HERMES
2458474.3154	-28.44	-0.57	-10.36	0.53	14.88	1.39	NRES
2458475.3148	-28.12	0.00	-18.55	0.09	22.91	0.34	HERMES
2458476.3158	-28.18	0.05	-18.67	0.53	23.28	1.30	NRES
2458478.2921	-27.85	-0.37	-13.50	0.56	17.07	1.45	NRES
2458478.2998	-27.86	-0.16	-13.61	0.27	17.49	0.31	NRES
2458478.3074	-27.87	-1.39	-12.37	0.36	18.33	0.32	NRES
2458493.3020	-24.38	-0.30	3.85	0.61	-3.05	1.52	HARPSN
2458494.3047	-24.10	-0.30	13.53	0.61	-14.71	1.54	HARPSN
2458495.3095	-23.82	-0.30	28.73	0.55	-32.12	1.46	HARPSN
2458496.3184	-23.53	-0.30	44.43	0.55	-50.77	1.46	HARPSN

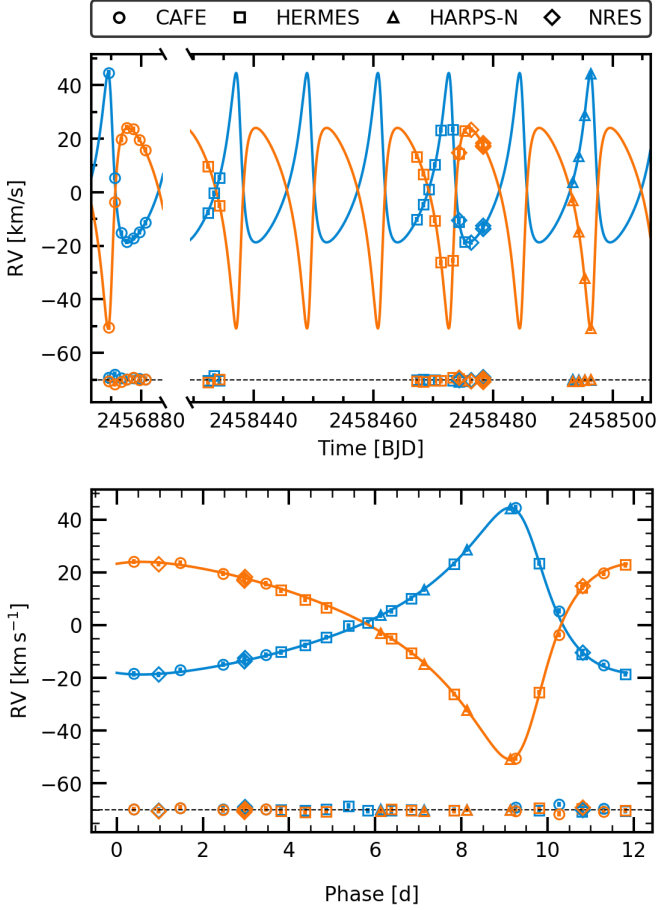


Fig. 8. RV values for the four different spectrographs (CAFE, HERMES, HARPS-N, and NRES) and orbital solution for the primary (blue) and secondary (orange) component of GJ 1284 as a function of time (*top panel*) and orbital phase (*bottom panel*). The residuals of the Keplerian fit calculated with *rvfit* are shown at the bottom of each panel using the same scale.

the one used in the literature to determine the membership of this object to a YMG (Sect. 2). Nonetheless, we note that the individual RV measurements derived by various authors all fall within the range of expected RV values for the primary component at different orbital phases.

We also compare the orbital period and eccentricity of this system against other spectroscopic binaries from Pourbaix et al. (2004) in Fig. 9. We note that the orbit of GJ 1284 is highly eccentric for its orbital period, lying close to the upper envelope (solid black line) defined by the binaries of the sample.

4.3. Rotational period determination

We determined the rotational period of the three systems from the TESS photometric time series (Sect. 3.2). First, we calculated the generalised Lomb-Scargle (GLS) periodogram (Zechmeister & Kürster 2009) of the photometry and identify the most significant peaks (see central panels of Fig. 7). Then, we visually inspected the photometric data folded with the period corresponding to the highest peak. In Fig. 7 we can see that GJ 898 presents a well-defined modulation with a two-peak pattern that is responsible for the peaks at 10.99 and 6.19 days in the periodogram. However, we find visually that the dispersion in the phase-folded light curve is minimised for a period of 11.5 ± 0.1

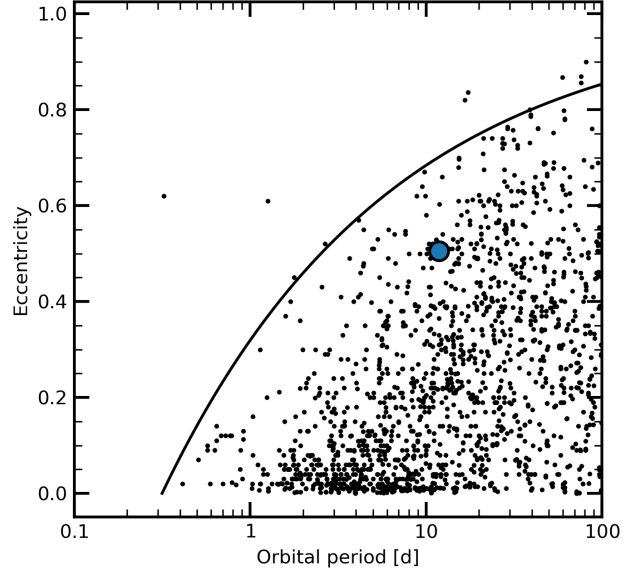


Fig. 9. Eccentricity and rotation period of GJ 1284 (in blue) against binary systems from Pourbaix et al. (2004). The black solid line represents the upper envelope for this distribution.

Table 5. Parameters of the simultaneous Keplerian fit to both components of GJ 1284 from *rvfit*.

Parameter	Limits	Value
<i>Fitted parameters</i>		
P [d]	[11.8, 11.9]	11.838033 ± 0.000016
t_{peri} [BJD]	–	2449997.0000 ± 0.0012
e	[0.0, 0.6]	0.505 ± 0.005
ω [°]	–	40.9 ± 0.3
γ [km s^{-1}]	[–15, 10]	0.84 ± 0.14
K_1 [km s^{-1}]	[20, 50]	31.6 ± 0.3
K_2 [km s^{-1}]	[20, 50]	37.4 ± 0.3
<i>Derived quantities</i>		
$M_1 \sin^3 i$ [M_{\odot}]		0.141 ± 0.003
$M_2 \sin^3 i$ [M_{\odot}]		0.119 ± 0.003
$q \equiv (M_1/M_2)$		0.845 ± 0.012
$a_1 \sin i$ [R_{\odot}]		6.38 ± 0.07
$a_2 \sin i$ [R_{\odot}]		7.56 ± 0.07
<i>Other quantities</i>		
χ^2		19.665861
Time span [day]		1621.6930
rms ₁ [km s^{-1}]		0.6175
rms ₂ [km s^{-1}]		0.5919

days, well within the width of the 10.99 days peak, adopting this value as the rotational period of GJ 898. On the contrary, GJ 1284 and GJ 897AB present a more complex pattern that can be attributed to the overlapping of the modulation of each component of these two binaries. Both stars also show intense flare activity, cropped out in Fig. 7 for clarity.

For GJ 897AB, we find that the shape of the light curve is quite different in the two TESS sectors. In Sector 2 (in blue in

Fig. 7) we find an irregular modulation with a two-peak pattern showing two main peaks at 5.32 and 2.43 days in the periodogram. In contrast, the light curve for Sector 29 (in red) shows a clear modulation with a period of 5.02 days. The periodogram of the combined light curves of the two sectors (in black) shows a peak at 5.00 days. This suggests that the periodicity at ~ 5 days in the light curve is due either to the individual components or to both of them, assuming they have similar rotational period given their similar spectral types and masses. Thus, we adopted a value of 5.00 ± 0.02 d as the rotational period of this system.

The light curve of GJ 1284 also shows a different behaviour for each sector, similarly to GJ 897. The light curve of Sector 2 (in blue) presents a more complex structure, while in Sector 29 it is more regular. The periodograms of both sectors have a main peak at around ~ 7.5 days. We expect a shorter rotation period for the secondary component than for the primary, given its later spectral type (Sect. 5.3.1), which we do not detect in the TESS light curve as it probably appears diluted due to its lower brightness (Sect. 5.3.2). Thus, we determine a rotational period for GJ 1284A of 7.5 ± 0.1 days.

We followed the same procedure described in this section to calculate the rotation period of the LA members from Montes et al. (2001). First, we cross-matched all 120 members with the *Gaia* eDR3 with a matching radius of $2''$ accounting for their proper motions to determine the new positions at the *Gaia* equinox (J2015.5). We rejected those matches that do not provide a full astrometric solution and radial velocity in *Gaia*, ending up with a total of 88 stars, for which we derived the UVW velocities and checked that their kinematics are still compatible with a membership to the LA. Of these 88 stars, 86 have two-minute-cadence TESS light curves available, but we can only recover a reliable measure of the rotation period for 64 of them, which are listed in Table 10 and plotted in yellow in Fig. 10c.

5. Discussion

5.1. Youth assessment

GJ 1284 has been proposed as a member of β PMG (~ 25 Myr; Binks & Jeffries 2014; Malo et al. 2014b) and COL (~ 40 Myr; Torres et al. 2008; Bell et al. 2015) (Sect. 2). Furthermore, its two wide companions have been kinematically assigned to LA (10–300 Myr; López-Santiago et al. 2009) (Sect. 2.2). The membership of GJ 1284 to one of these groups, and thus its age, is fundamental so it can be compared with stellar evolutionary models.

We calculated the UVW galactocentric velocities from the revised systemic RV γ (Sect. 4.2) and the astrometry from the *Gaia* eDR3 using the transformations described in Johnson & Soderblom (1987). We also revised the kinematics of GJ 898 using the astrometry and RV from *Gaia* eDR3. Moreover, we calculated the 3D space motions of GJ 897AB with the astrometry from Tokovinin (2018) and the RV from Torres et al. (2006) (Sect. 2.2). We show the revised UVW velocities in Fig. 1 and list the values in Table 2. The kinematics of all three systems agree and are compatible with other members of LA from Montes et al. (2001). Moreover, our determination of the systemic velocity of GJ 1284 place this object outside β PMG and COL as defined in the BANYAN- Σ code (Gagné et al. 2018).

We employed several youth indicators to further constrain the kinematic age, including the $H\alpha$ pseudo-equivalent width $pEW(H\alpha)$, the near-ultraviolet (NUV) excess emission measured with the colour $NUV - J$, the X-ray luminosity L_X , the stellar rotational period, and the pEW of the Li feature at 6707.8 nm.

In the upper left panel of Fig. 10 we show that all three objects present $H\alpha$ emission compatible with members of the Pleiades (~ 110 – 130 Myr; Stauffer et al. 1998; Dahm 2015), but also with some stars from the Hyades (~ 650 – 800 Myr; Martín et al. 2018; Douglas et al. 2019; Lodieu 2020, and references therein) according to Fang et al. (2018). We set the age range of the systems between the estimated age of these two open clusters.

From the 2MASS (Skrutskie et al. 2006) J and K magnitudes and the GALEX (Martin et al. 2005) NUV magnitude (Table 2), we inferred colours $J - K = 0.871, 0.763, 0.854$ mag and $NUV - J = 11.689, 11.427, 11.395$ mag for GJ 1284, GJ 898, and GJ 897, respectively. Findeisen et al. (2011) identified a correlation between age and NUV excess emission for members of YMGs. The $NUV - J$ colours of our objects indicate an excess emission in the NUV compatible with members of YMGs younger than the Hyades (see Figures 7, 8, and 9 in Findeisen et al. 2011).

We derived a $\log(L_X) = 28.15, 28.74, 28.92$ erg s $^{-1}$ for GJ 898 and the individual components of GJ 1284AB and GJ 897AB, respectively, assuming comparable X-ray luminosities for the two components of the binary systems. These levels of X-ray emission are compatible with objects younger than the Hyades (Núñez & Agüeros 2016), as shown in the upper right panel of Fig. 10.

We compared the rotational periods of GJ 1284A, GJ 898, and GJ 897A against members of the Pleiades and Praesepe open clusters from Rebull et al. (2016) and Douglas et al. (2016, 2019), respectively (Fig. 10). We calculated the $G - J$ colour of GJ 897A assuming that the two components have similar spectral types. As for GJ 1284, the method for calculating the colour of its binary components is described in detail in Sect. 5.3.1.

The lower left panel of Fig. 10 shows that the rotational periods of the three stars are longer than the values expected for members of the Pleiades, but shorter than for members of Praesepe (~ 600 – 750 Myr; Douglas et al. 2019, and references therein). From the rotational period, we conclude that the age of these three systems is most likely bracketed by the age of the two open clusters. We note that the rotational period of GJ 1284 might be affected by the tidal interaction between the two components. Simulations show that the spin and orbit of binary systems with orbital periods of less than 10 days might synchronise on a timescale as short as 200 Myr (Fleming et al. 2019). However, this is not the case for GJ 1284AB as its orbital period is roughly 1.5 times longer than the rotational period of the primary component. In any case, the conclusions of the age determination derived from the rotational period of GJ 898 and GJ 897A still hold.

We found no presence of the Li6708 line in our GJ 1284 spectra similarly to Torres et al. (2006) setting an upper limit of $pEW_{Li6708} < 35$ mÅ from our spectra. We also analysed an archival HARPS spectra for GJ 898 (programme 085.C-0019(A); PI: Lo Curto) again finding no sign of the Li6708 line, determining an upper limit for its $pEW_{Li6708} < 17$ mÅ. This indicates that their age must be older than IC 2602 (40–50 Myr Dobbie et al. 2010), and that it is compatible with members of the Pleiades (Gutiérrez Albarrán et al. 2020) or older, as shown in the lower right panel of Fig. 10.

We can also put constraints on the age of the GJ 1284 based on the high eccentricity of its orbit (Table 5). Meibom & Mathieu (2005) determined a relation of the circularisation period with age from binary members of several open clusters. Although the Hyades cluster appears as an outlier in the original work, a revi-

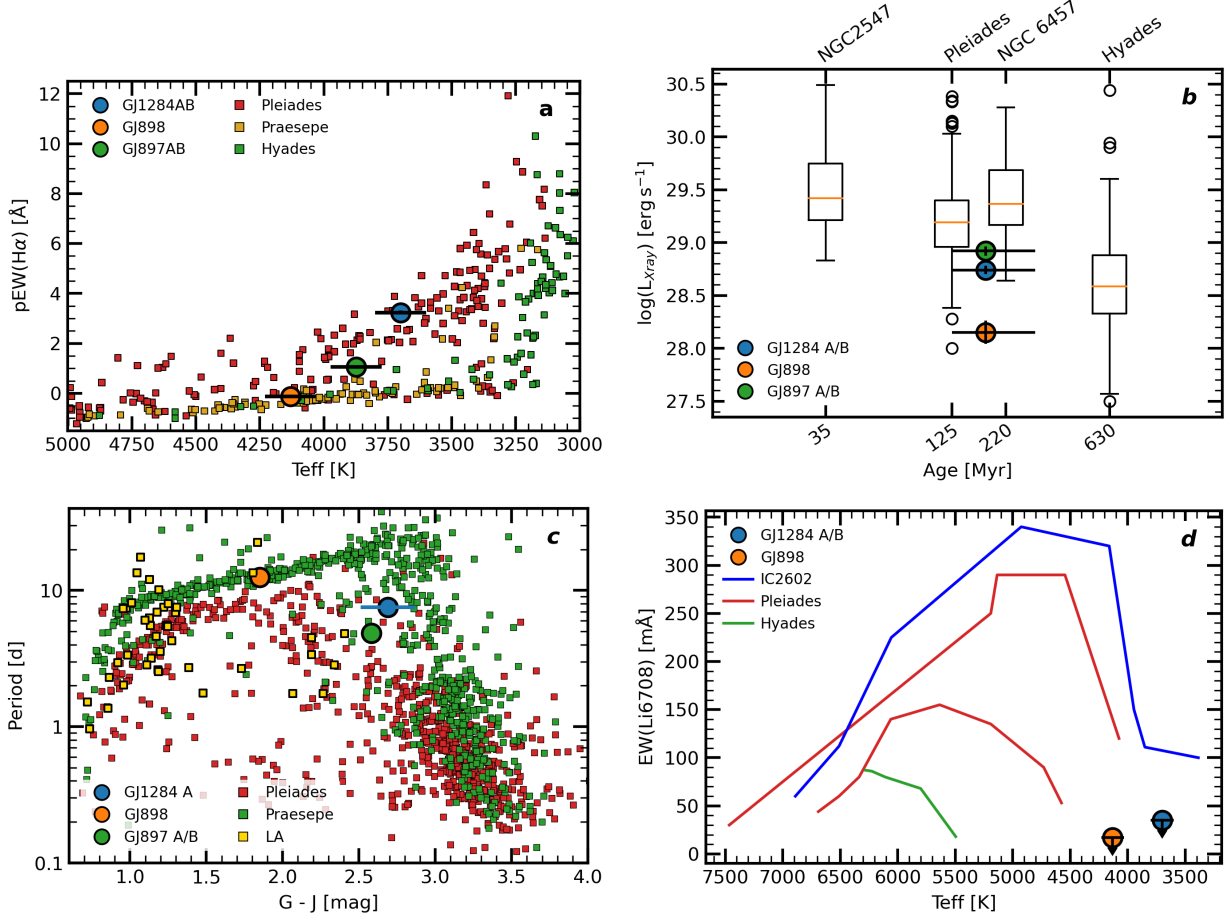


Fig. 10. Comparison of the values of four different youth indicators for the three systems analysed in this work (GJ 1284, GJ 898, GJ 897) against young objects from the literature. *Panel a:* Pseudo-equivalent width of the H α line against members of the Pleiades, Praesepe, and Hyades open clusters from Fang et al. (2018); *Panel b:* X-ray luminosity of the individual components compared with members from four different open clusters from Núñez & Agüeros (2016) presented in a box-plot; *Panel c:* Rotational period derived from the TESS light curves alongside a compilation of members of the Pleiades from Rebull et al. (2016) and of the Hyades from Douglas et al. (2016), and rotational periods for LA members in Montes et al. (2001) derived in this work (see Sect. 5.1); *Panel d:* Upper limits of the EW of the Li 6708 Å feature plotted alongside the upper envelopes of the IC 2602 and Hyades open clusters, as well as the upper and lower envelopes of the Pleiades (Gutiérrez Albarrán et al. 2020, and references therein)

sion of the binaries used in the analysis showed that the cut-off period for this open cluster is in fact 8.5–11.9 days (see Gillen et al. 2017, for more details). The Hyades upper limit is similar to the orbital period of our system (Table 5), thus we infer that it must be younger than the age of this open cluster, which agrees with the expected age derived from the other youth indicators. Moreover, we note again the high eccentricity of the orbit, which can be seen in Fig. 9 where GJ 1284AB is located near the upper envelope, indicating that it is still far from being circularised and suggesting that it is well below the age of the Hyades.

We summarise the age range estimated from the lower limit of the younger age and the upper limit from the older age for each activity indicator in Table 6. The upper limit is set by the estimated maximum age of the stellar associations part of LA. In Fig. 10c we see that the rotation periods of the LA members from Table 10 (in yellow) lie mostly between the sequences defined by the Praesepe and Pleiades stars, which is consistent with the estimated age range of 10–300 Myr from the literature. However, we also note that some of them follow the Praesepe sequence or are located slightly above it. This leads us to believe that the upper limit for the age of this association is not well constrained, although it is indeed young. Given that the main conclusions from

this work are drawn from the fact that the objects have arrived to the main sequence (see Sect. 5.3.1), which is firmly based on the lower limit for the age imposed by the rotational period, the upper limit for the age of LA does not affect them. Here we adopt a maximum age for the LA similar to those of Praesepe and Hyades. The estimated age ranges for the different indicators are then compatible with an age for the system of 110–800 Myr.

5.2. Gravitational bond of the quintuple system

Throughout Sect. 5.1 and in the following Sect. 5.3.1 we work under the assumption that GJ 1284 and its two wide companions, GJ 898 and GJ 897AB, have a common origin based on their kinematics and thus are roughly the same age. Even though the youth indicators and kinematics support the membership of these three systems to the LA, given the wide age range of this YMG we cannot confirm they have the same age. Moreover, the wide physical separation of 1.66 pc between them might indicate that they are not physically bound.

To explore the different scenarios, we first determine the probability of finding two members of the LA with physical separations and velocities as similar as GJ 1284 and GJ 898 based on

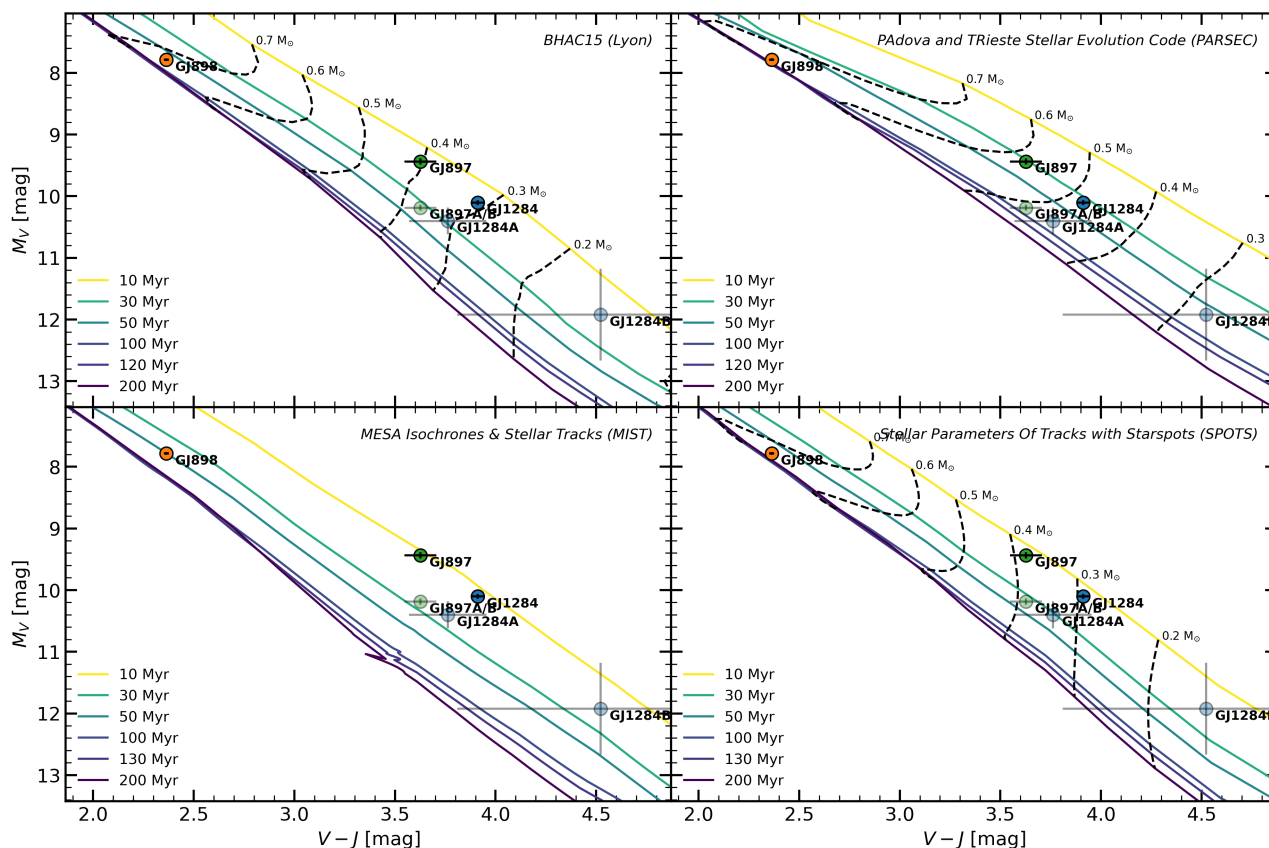


Fig. 11. Comparison of the measured magnitudes for GJ 1284, GJ 898, and GJ 897 and the calculated magnitude for the individual components of the two binary systems against a set of isochrones from four different PMS evolutionary models: BHAC15 (top left), PARSEC (top right), MIST (bottom left), and SPOTS (bottom right). We also include the isomasses (dashed lines) for each of the models for initial mass values ranging from 0.7 to 0.2 M_{\odot} .

Table 6. Summary of the possible age ranges for GJ 1284 according to the different youth indicators considered in this work.

Youth indicator	Age [Myr]
Kinematics	10–800 ^a
H α emission	< 800
NUV excess emission	< 800
X-ray luminosity	< 800
Rotational period	110–750
Li 6708Å	> 50
Final	110–800

Notes. ^(a) The upper limit for the age of the LA members is derived from a comparison of the rotation periods of its members with open clusters. See Sect. 5.1 for more details.

the galactocentric positions and velocities of the members from Montes et al. (2001). We estimate that the probability that two of them have UVW velocities as similar as our systems is ~ 10 –15%, depending on whether we select all the LA members or only the denser region in the UVW velocity space. Furthermore, the probability that two LA members are closer than 1.66 pc is lower than 0.2%, given that members of YMGs are not grouped as in open clusters, but instead are dispersed over a much larger volume. Thus, the combined probability of finding two systems at these separations in the position and velocity space is only 0.05% or less.

We also calculate the disruption times of our system to test the hypothesis that they are physically bound using the expressions from Weinberg et al. (1987) and Binney & Tremaine (1987). For this calculation we adopt a mean mass for the eventual perturber of $1 M_{\odot}$, a system density of 0.078 – 0.084 pc^{-3} (Henry et al. 2018) and a mean velocity dispersion for the perturbers of 59.8 km s^{-1} (Zapatero Osorio et al. 2007) for the solar neighbourhood, together with the masses for GJ 898 ($\sim 0.66 M_{\odot}$) and GJ 1284AB ($\sim 0.77 M_{\odot}$, see Sect. 5.3.2) and their separation (1.66 pc). With these parameters we derive a disruption time $t_{\text{disr}} \approx 100$ – 200 Myr , which is comparable to the age estimated from the youth indicators (Sect. 5.1) suggesting that the system might still be physically bound. However, the difference in the W velocities of GJ 1284 and GJ 898, an order of magnitude higher than the escape velocity of the latter of $\sim 100 \text{ m s}^{-1}$, indicates otherwise. Nonetheless, if we trace back the motion of these two systems using their UVW velocities, we find that they reached their minimum separation (0.6 pc) just $1.3 \pm 0.5 \text{ Myr}$ ago. Using this distance instead, we infer a disruption time $t_{\text{disr}} \approx 400$ – 700 Myr , longer than the time we calculated previously, but still comparable to the age of the system. In summary, although currently the system does not seem to be physically bound, we believe that it is very unlikely to find such relatively close systems in the LA by chance alignment. Additionally, we cannot rule out that the system was physically bound until 1–2 Myr ago when it could have been disrupted by an impact from a perturber.

5.3. Model comparison

5.3.1. Colour-magnitude diagrams

In this section we compare the absolute magnitudes and colours of the three systems with four different PMS evolutionary models: Lyon models (BHAC15; Baraffe et al. 2015); MESA Isochrones & Stellar Tracks (MIST; Dotter 2016; Choi et al. 2016); PAdova and TRIeste Stellar Evolution Code (PARSEC; Bressan et al. 2012; Chen et al. 2014); and Stellar Parameters of Tracks with Starspots (SPOTS; Somers et al. 2020). A brief description of the characteristics of each of these models can be found in David et al. (2019). In Fig. 11 we plot the absolute V magnitudes and the $V - J$ colour of each system, and of their individual components together with the isochrones from each theoretical model.

To separate the integrated photometry of GJ 1284 into the corresponding magnitudes for the individual components we use the integrated *Gaia* G_{BP} magnitude and the flux ratio derived by TODMOR from the HARPS-N spectra. The wavelength range of the HARPS-N spectra closely resembles the transmission curve of the G_{BP} filter⁵, hence justifying this approximation. The absolute G_{BP} is calculated from the parallax of this object (Table 2). Using these values, we derive absolute magnitudes in the G_{BP} filter of 10.73 ± 0.09 and 11.55 ± 0.13 mag for the primary and secondary components, respectively. Additionally, we use the relations for old field stars from Pecaut & Mamajek (2013)⁶ assuming that the system is close to the main sequence based on its age (Sect. 5.1). We base this approximation on the fact that, for solar-type stars and early- to mid-type M dwarfs, the isochrones of the evolutionary models for ages older than ~ 120 Myr, as our objects appear to be, squeeze together (Fig. 11). Moreover, a comparison with empirical masses and luminosities of members of the NGC 1647 (~ 150 Myr; Dias et al. 2002), Pleiades, and Praesepe open clusters with similar spectral types (Sect. 5.3.2) show that the mass-luminosity sequences overlap at this range of ages. According to the G_{BP} absolute magnitude, we infer a spectral type of M2–M2.5 and M3–M3.5 respectively for the primary and secondary components of GJ 1284 using these relations. We estimate the difference in magnitudes between the two components for the different filters from these same relations and decompose the other integrated photometry into the individual magnitudes. We take into account the uncertainties in the spectral type estimates to calculate the photometric error bars. For GJ 897AB, the two components of the binary system have similar spectral types (Sect. 2.2), hence we assume identical fluxes.

Figure 11 shows that the BHAC15, MIST, and SPOTS models predict a younger isochronal age for GJ 1284A/B and GJ 897A/B (~ 30 – 50 Myr) than for GJ 898 (~ 100 Myr). This effect was already noticed by Herczeg & Hillenbrand (2015) using the BHAC15 models, which predicted younger ages for very low-mass stars than for solar-type stars in other YMGs. In Table 7 we also list the isochronal age calculated minimising the combined distance of the three systems to each isochrone assuming they are coeval. To account for the uncertainties in the magnitude and colour of the individual components we performed a Monte Carlo simulation with 5 000 realisations to estimate the error in the age determination. We see that these ages are younger than those derived from the youth indicators in Sect. 5.1, in particular from the rotational period. The determination of

Table 7. Summary of the isochronal ages for each model derived for the three systems analysed in this work, assuming coevality.

	BHAC15	PARSEC	MIST	SPOTS
Age [Myr]	35^{+25}_{-14}	72^{+67}_{-35}	30^{+25}_{-13}	42^{+48}_{-22}

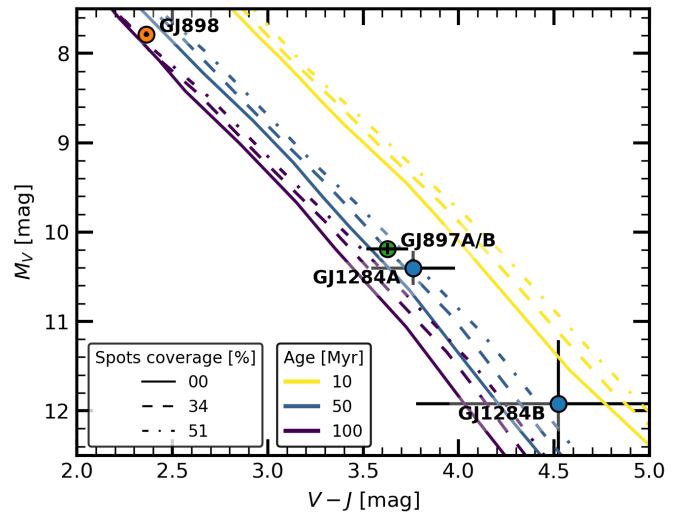


Fig. 12. Isochrones from the SPOTS model for three different ages (10, 50, and 100 Myr) and different spot-filling factors (0, 34, and 51%).

isochronal ages younger than expected for members of other young associations was also noted in other works (e.g. David et al. 2016; Gillen et al. 2017). On the other hand, PARSEC models suggest a common age of ~ 40 – 140 Myr for all of them, consistent with the youth indicators. The version v1.2S of the PARSEC models considered in this work includes an ad hoc correction to reconcile the models with the observational data, particularly for very low-mass stars (Chen et al. 2014). This might explain the differences between PARSEC and the other three sets of models.

The discrepancy in the age derived by the different models indicates that there might be an additional factor that varies for the three systems. For example, the SPOTS models include the effects of magnetic fields in the form of stellar spots, while the other models do not (Somers et al. 2020). Somers & Pinsonneault (2015) explored in detail the effect of spot-related activity in the stellar evolution and found that low-mass stars with starspots have lower luminosities and temperatures compared to those with no spots. As a consequence, ages in spotted stars can be underestimated by a factor of 2–10. However, the spot-filling factor cannot be directly determined from our observations. In Fig. 12 we show isochrones derived from the SPOTS models for different spot-filling factors. We can see for the typical maximum value of 50% in PMS low-mass stars (Somers & Pinsonneault 2015 and reference therein) that the isochronal ages of the three systems are in better agreement with the lower limit for the age ~ 100 Myr derived from the youth indicators and the values derived by the PARSEC models.

5.3.2. Mass-luminosity relations

In this section we compare the minimum masses of GJ 1284A and B (Sect. 4.2) and other dynamical mass determinations with the predictions from the PMS models in a mass-luminosity dia-

⁵ https://www.cosmos.esa.int/web/gaia/iow_20180316

⁶ See updated version including Sloan and *Gaia* filters in http://www.pas.rochester.edu/~emamajek/EEM_dwarf_UBVIJHK_colours_Teff.txt

Table 8. Summary of maximum and minimum masses (in M_{\odot}) of the two binary components derived from the isochrones of the different models.

Model	Primary		Secondary	
	Min	Max	Min	Max
BHAC15	0.427	0.452	0.361	0.382
PARSEC	0.444	0.479	0.375	0.404
MIST	0.422	0.440	0.356	0.372
SPOTS	0.435	0.456	0.367	0.385

gram (Fig. 13). We use the bolometric corrections from Pecaut & Mamajek (2013) for the spectral types of the individual components and the G_{BP} magnitudes of GJ 1284A and B (Sect. 5.3.1) to derive a bolometric luminosity of $\log(L_{\text{bol}}/L_{\odot}) = -1.61 \pm 0.05$ and -1.77 ± 0.09 for the primary and the secondary components, respectively. These values for the luminosities and the minimum masses are compatible with the theoretical mass-luminosity relations.

Given the bolometric luminosity of the individual components of GJ 1284, we can estimate their masses using the mass-luminosity relations from the models assuming an age range for the system of 110–800 Myr (Sect. 5.1) obtaining a mean mass of 0.432–0.462 M_{\odot} and 0.365–0.390 M_{\odot} for the primary and secondary, respectively. The intervals of masses for each model (Table 8) take into account the estimated range of ages. We compare these results with dynamical masses measured for EBs with similar ages and spectral types (Fig. 13) from a compilation by Lodieu et al. (2020), namely with members of the Pleiades (in red) from David et al. (2016) and Hebb et al. (2006) and Praesepe (in green) from Kraus et al. (2017) and Gillen et al. (2017) with spectral types M2–M4 for at least one of their components. We see that the masses derived for GJ 1284A and B from their luminosity and age are consistent with the dynamical masses for these EBs, and in particular they seem to be delimited between the masses of 2MASSJ0446+19A (M2.5V; $0.47 \pm 0.05 M_{\odot}$; Hebb et al. 2006) and PTFEB132.707+19.810 (M3.5V; $0.3953 \pm 0.0020 M_{\odot}$; Kraus et al. 2017), whose spectral types are also compatible with the GJ 1284 components (Sect. 5.3.1). Assuming that the masses of each component derived from the photometry are correct, they imply an inclination angle for the orbit of the binary system of $43.6\text{--}42.8^{\circ}$ or $43.5\text{--}42.3^{\circ}$ according to the minimum mass of primary and the secondary, respectively.

We can also see, with the exception of PARSEC, that the masses derived from the mass-luminosity relations for each model are higher than the values inferred from the CMD for the same model. Moreover, the masses derived from the CMD are lower than the dynamical masses from the literature. The colour and magnitude corrections needed to reconcile the masses derived from the mass-luminosity relations and the CMDs are listed in Table 9. This suggests that the mass-luminosity relations seem to be more reliable to derive masses from the photometry than CMDs. One of the possible explanations for this could be that, although the evolutionary models may correctly predict the values of the luminosities, they appear to underestimate the effective temperatures. This was already noted in other works (David et al. 2016; Gillen et al. 2017), where models predicted effective temperatures 200–300 K hotter for early to mid M dwarfs. Alternatively, model atmospheres and spectral synthesis for these objects may predict magnitudes and colours for these very cool objects that are not fully correct. Furthermore,

Table 9. Colour and magnitudes differences needed to reconcile the mass estimates derived from the CMD and the mass-luminosity relations for each model.

Model	Primary		Secondary	
	ΔM_V [mag]	$\Delta(V-J)$ [mag]	ΔM_V [mag]	$\Delta(V-J)$ [mag]
BHAC15	0.13	0.48	1.03	1.02
PARSEC	-0.08	0.19	0.64	0.62
MIST	0.27	0.67	1.16	1.21
SPOTS	0.05	0.41	0.89	0.90

Notes. The uncertainties associated with these colour and magnitude differences are dominated by the error on the magnitudes (0.19, 0.71 mag) and the colours (0.21, 0.74 mag) of the primary and secondary components, respectively.

this also indicates that, unless the age of the system is younger than the value derived from the youth indicators in this work, only the PARSEC models seem to predict masses consistent with those derived from mass-luminosity relations and CMDs and also compatible with empirical masses of EBs in open clusters older than 100 Myr.

6. Conclusions

In this work we analyse a young SB2 system, GJ 1284, alongside its two wide companion, GJ 898 and GJ 897AB, and compare the results of this analysis with several PMS evolutionary models. The main results and conclusions from this work are as follows:

- We characterised the orbit of GJ 1284, a young SB2 system, using RVs derived using high-resolution spectra from HERMES, HARPS-N, CAFE, and NRES. We find that this system is composed of two stars of similar mass ($q = 0.845 \pm 0.012$) with estimated spectral types of M2–M2.5 for the primary component and M3–M3.5 for the secondary in an eccentric orbit ($e = 0.505 \pm 0.005$) with a period of $P = 11.838033 \pm 0.000016$ d. We also derived a minimum mass of 0.141 ± 0.003 , $0.119 \pm 0.003 M_{\odot}$ for the primary and secondary components, respectively.
- We re-analysed the kinematics of GJ 1284AB using the revised systemic velocity of $0.84 \pm 0.14 \text{ km s}^{-1}$, which suggests a membership in the LA, consistent GJ 898 and GJ 897AB, in the same YMG. Based on several youth indicators, we adopted an age range for the three systems of 110–800 Myr, assuming they have a common origin.
- We find that the probability of finding a system such as the one made up of GJ 1284 and its two relatively close co-moving companions in the LA by chance alignment is very low, suggesting they might have a common origin. Moreover, although currently they do not seem to be physically bound, we cannot rule out that they were in the past before being disrupted just 1–2 Myr ago.
- We find that the isochronal ages derived from the comparison of the photometry with four PMS evolutionary models (BHAC15, PARSEC, MIST, and SPOTS) derived from the photometry of these three systems are younger than those estimated from the youth indicators, except for the PARSEC models. Moreover, the isochrones of the models, again excluding PARSEC, suggest a different age for the early M dwarf binaries than for the solar-type star.

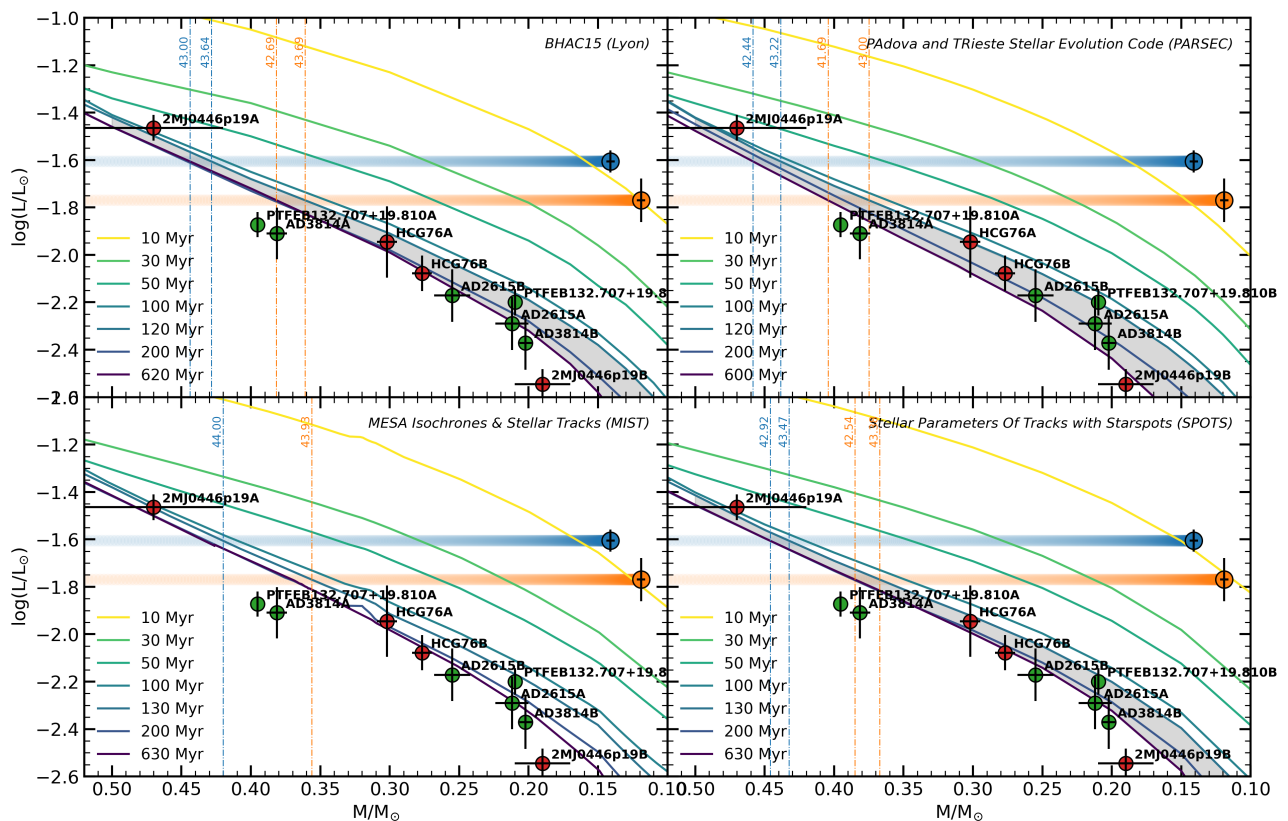


Fig. 13. Minimum masses and luminosities of GJ 1284 A (blue) and B (orange) against the mass-luminosity relations derived from the BHAC15 (top left), PARSEC (top right), MIST (bottom left), and SPOTS (bottom right) models. The blue and orange horizontal bars represent the expected masses at different inclination angles for the primary and the secondary components, respectively. The dashed vertical lines indicate the masses derived from the mass-luminosity relations for the minimum and maximum ages derived from the youth indicators (shaded in grey). For comparison, we overplot the dynamical masses of the EB members of NGC 1647, the Pleiades (red) and Praesepe (green) open clusters from Lodieu et al. (2020).

- Finally, we see that the masses for GJ 1284 A and B from the mass-luminosity relations for the different evolutionary models, except PARSEC, are higher than the values derived from the photometry alone, but are consistent with the dynamical masses of EBs with similar spectral type and age from the literature. This suggests that the determination of masses using mass-luminosity relations from evolutionary models may be more reliable than a comparison with the photometry in CMDs. Alternatively, the system might be younger than we estimated from the youth indicators.

Acknowledgements. We thank the anonymous referee for his/her comments that helped to improve this work. CCG is supported by the Ministerio de Economía y Competitividad del Gobierno de España (MINECO) under project SEV-2015-0548-16-3. We acknowledge financial support from the Agencia Estatal de Investigación of the Ministerio de Ciencia, Innovación y Universidades through projects PID2019-109522GB-C5[3, 4] and AEI/10.13039/501100011033. Based on observations made with the Mercator Telescope, operated on the island of La Palma by the Flemish Community, at the Spanish Observatorio del Roque de los Muchachos of the Instituto de Astrofísica de Canarias. Based on observations obtained with the HERMES spectrograph, which is supported by the Research Foundation - Flanders (FWO), Belgium, the Research Council of KU Leuven, Belgium, the Fonds National de la Recherche Scientifique (F.R.S.-FNRS), Belgium, the Royal Observatory of Belgium, the Observatoire de Genève, Switzerland and the Thüringer Landessternwarte Tautenburg, Germany. This work has made use of data from the European Space Agency (ESA) mission *Gaia* (<https://www.cosmos.esa.int/gaia>), processed by the *Gaia* Data Processing and Analysis Consortium (DPAC, <https://www.cosmos.esa.int/web/gaia/dpac/consortium>). Funding for the DPAC has been provided by national institutions, in particular the institutions participating in the *Gaia* Multilateral Agreement. This work makes use of observations from the NRES spectrograph on the LCOGT 1m telescope at the SAAO node of the Las Cumbres

Observatory global telescope network. Based on observations made with the Italian Telescopio Nazionale Galileo (TNG) operated on the island of La Palma by the Fundación Galileo Galilei of the INAF (Istituto Nazionale di Astrofisica) at the Spanish Observatorio del Roque de los Muchachos of the Instituto de Astrofísica de Canarias. Based on observations collected at the Centro Astronómico Hispano-Alemán (CAHA) at Calar Alto, operated jointly by Junta de Andalucía and Consejo Superior de Investigaciones Científicas (IAA-CSIC). This paper includes data collected by the TESS mission. Funding for the TESS mission is provided by the NASA's Science Mission Directorate. This publication makes use of data products from the Two Micron All Sky Survey, which is a joint project of the University of Massachusetts and the Infrared Processing and Analysis Center/California Institute of Technology, funded by the National Aeronautics and Space Administration and the National Science Foundation.

References

- Aceituno, J., F Sánchez, S., Grupp, F., et al. 2013, *A&A*, 552, A31
 Asiain, R., Figueras, F., Torra, J., & Chen, B. 1999, *A&A*, 341, 427
 Baglin, A., Auvergne, M., Boissard, L., et al. 2006, in 36th COSPAR Sci. Assem., 3749
 Baraffe, I., Homeier, D., Allard, F., & Chabrier, G. 2015, *A&A*, 577, A42
 Barrado y Navascués, D., Stauffer, J. R., Song, I., & Caillault, J.-P. 1999, *ApJ*, 520, L123
 Bell, C. P. M., Mamajek, E. E., & Naylor, T. 2015, *Mon. Not. R. Astron. Soc.*, 454, 593
 Binks, A. S. & Jeffries, R. D. 2014, *Mon. Not. R. Astron. Soc. Lett.*, 438, L11
 Binney, J. & Tremaine, S. 1987, *Galactic dynamics* (Princeton, N.J.: Princeton University Press, c1987)
 Borucki, W., Koch, D., Basri, G., et al. 2007, *Proc. Int. Astron. Union*, 3, 17
 Bressan, A., Marigo, P., Girardi, L., et al. 2012, *Mon. Not. R. Astron. Soc.*, 427, 127
 Brown, A. G., Vallenari, A., Prusti, T., & de Bruijne, J. H. 2020, *A&A*, 1

- Brown, T. M., Baliber, N., Bianco, F. B., et al. 2013, *Publ. Astron. Soc. Pacific*, 125, 1031
- Chen, Y., Girardi, L., Bressan, A., et al. 2014, *Mon. Not. R. Astron. Soc.*, 444, 2525
- Choi, J., Dotter, A., Conroy, C., et al. 2016, *ApJ*, 823, 102
- Cosentino, R., Lovis, C., Pepe, F., et al. 2014, in *Ground-based Airborne Instrum.* Astron. V, ed. S. K. Ramsay, I. S. McLean, & H. Takami, 91478C
- Cosentino, R., Lovis, C., Pepe, F., et al. 2012, in *Ground-based Airborne Instrum.* Astron. IV, ed. I. S. McLean, S. K. Ramsay, & H. Takami No. September, 84461V
- Dahm, S. E. 2015, *ApJ*, 813, 108
- David, T. J., Conroy, K. E., Hillenbrand, L. A., et al. 2016, *Astron. J.*, 151, 112
- David, T. J., Hillenbrand, L. A., Gillen, E., et al. 2019, *ApJ*, 872, 161
- Dias, W. S., Alessi, B. S., Moitinho, A., & Lépine, J. R. D. 2002, *A&A*, 389, 871
- Dobbie, P. D., Lodieu, N., & Sharp, R. G. 2010, *Mon. Not. R. Astron. Soc.*, 409, 1002
- Dotter, A. 2016, *Astrophys. J. Suppl. Ser.*, 222, 8
- Douglas, S. T., Agüeros, M. A., Covey, K. R., et al. 2016, *ApJ*, 822, 47
- Douglas, S. T., Curtis, J. L., Agüeros, M. A., et al. 2019, *ApJ*, 879, 100
- Dudorov, A. E. & Eretnova, O. V. 2016, *Astron. Astrophys. Trans.*, 29, 437
- Eggen, O. J. 1975, *Publ. Astron. Soc. Pacific*, 87, 37
- Elliott, P., Bayo, A., Melo, C. H. F., et al. 2016, *A&A*, 590, A13
- Fang, X.-S., Zhao, G., Zhao, J.-K., & Bharat Kumar, Y. 2018, *Mon. Not. R. Astron. Soc.*, 476, 908
- Findeisen, K., Hillenbrand, L., & Soderblom, D. 2011, *Astron. J.*, 142, 23
- Fleming, D. P., Barnes, R., Davenport, J. R. A., & Luger, R. 2019, *ApJ*, 881, 88
- Gagné, J., Mamajek, E. E., Malo, L., et al. 2018, *ApJ*, 856, 23
- Galicher, R., Marois, C., Macintosh, B., et al. 2016, *A&A*, 594, A63
- Gillen, E., Hillenbrand, L. A., David, T. J., et al. 2017, *ApJ*, 849, 11
- Gizis, J. E., Reid, I. N., & Hawley, S. L. 2002, *Astron. J.*, 123, 3356
- Gliese, W. & Jahreiss, H. 1991, *NASA STI/Recon Tech. Rep. A*, 224, 161
- Gutiérrez Albarrán, M. L., Montes, D., Gómez Garrido, M., et al. 2020, *A&A*, 643, A71
- Hawley, S. L., Gizis, J. E., & Reid, I. N. 1996, *Astron. J.*, 112, 2799
- Hebb, L., Wyse, R. F. G., Gilmore, G., & Holtzman, J. 2006, *Astron. J.*, 131, 555
- Heintz, W. D. 1986a, *Astron. Astrophys. Suppl. Ser.*, 65, 411
- Heintz, W. D. 1986b, *Astron. J.*, 92, 446
- Henden, A. A., Templeton, M., Terrell, D., et al. 2016, *VizieR Online Data Cat.*, II/336
- Henry, T. J., Jao, W.-C., Winters, J. G., et al. 2018, *Astron. J.*, 155, 265
- Herczeg, G. J. & Hillenbrand, L. A. 2015, *ApJ*, 808, 23
- Husser, T.-O., Wende-von Berg, S., Dreizler, S., et al. 2013, *A&A*, 553, A6
- Janson, M., Durkan, S., Hippler, S., et al. 2017, *A&A*, 599, A70
- Jeffers, S. V., Schöfer, P., Lamert, A., et al. 2018, *A&A*, 614, A76
- Johnson, D. R. H. & Soderblom, D. R. 1987, *Astron. J.*, 93, 864
- Jones, D. O. & West, A. A. 2016, *ApJ*, 817, 1
- Koch, D. G., Borucki, W., Dunham, E., et al. 2004, 1491
- Kraus, A. L., Douglas, S. T., Mann, A. W., et al. 2017, *ApJ*, 845, 72
- Kuiper, V. G. P. 1943, *ApJ*, 97, 275
- Lodieu, N. 2020, *Mem. della Soc. Astron. Ital.*, 91, 84
- Lodieu, N., Paunzen, E., & Zejda, M. 2020, in *Rev. Front. Mod. Astrophys.* (Cham: Springer International Publishing), 213–243
- López-Santiago, J., Micela, G., & Montes, D. 2009, *A&A*, 499, 129
- López-Santiago, J., Montes, D., Crespo-Chacon, I., & Fernandez-Figueroa, M. J. 2006, *ApJ*, 643, 1160
- López-Santiago, J., Montes, D., Gálvez-Ortiz, M. C., et al. 2010, *A&A*, 514, A97
- Makarov, V. V., Zacharias, N., & Hennessy, G. S. 2008, *ApJ*, 687, 566
- Malo, L., Artigau, É., Doyon, R., et al. 2014a, *ApJ*, 788, 81
- Malo, L., Doyon, R., Feiden, G. A., et al. 2014b, *ApJ*, 792, 37
- Malo, L., Doyon, R., Lafrenière, D., et al. 2013, *ApJ*, 762, 88
- Martin, D. C., Fanson, J., Schiminovich, D., et al. 2005, *ApJ*, 619, L1
- Martín, E. L., Lodieu, N., Pavlenko, Y., & Béjar, V. J. S. 2018, *ApJ*, 856, 40
- Mason, B. D., Hartkopf, W. I., Urban, S. E., et al. 2002, *Astron. J.*, 124, 2254
- Mayor, M., Pepe, F., Queloz, D., et al. 2003, *The Messenger*, 114, 20
- Meibom, S. & Mathieu, R. D. 2005, *ApJ*, 620, 970
- Meshkat, T., Mawet, D., Bryan, M. L., et al. 2017, *Astron. J.*, 154, 245
- Montes, D., López-Santiago, J., Gálvez, M., et al. 2001, *Mon. Not. R. Astron. Soc.*, 328, 45
- Myers, J. R., Sande, C. B., Miller, A. C., Warren, W. H., J., & Tracewell, D. A. 2015, *VizieR Online Data Cat.*, V/145
- Naud, M.-E., Artigau, É., Doyon, R., et al. 2017, *Astron. J.*, 154, 129
- Nielsen, E. L., De Rosa, R. J., Macintosh, B., et al. 2019, *Astron. J.*, 158, 13
- Núñez, A. & Agüeros, M. A. 2016, *ApJ*, 830, 44
- Pecaut, M. J. & Mamajek, E. E. 2013, *Astrophys. J. Suppl. Ser.*, 208, 9
- Piskunov, N. E. & Valenti, J. A. 2002, *A&A*, 385, 1095
- Pollacco, D. L., Skillen, I., Cameron, A. C., et al. 2006, *Publ. Astron. Soc. Pacific*, 118, 1407
- Pourbaix, D., Tokovinin, A. A., Batten, A. H., et al. 2004, *A&A*, 424, 727
- Prusti, T., de Bruijne, J. H. J., Brown, A. G. A., et al. 2016, *A&A*, 595, A1
- Raskin, G., Van Winckel, H., Hensberge, H., et al. 2011, *A&A*, 69, 1
- Rebull, L. M., Stauffer, J. R., Bouvier, J., et al. 2016, *Astron. J.*, 152, 113
- Riaz, B., Gizis, J. E., & Harvin, J. 2006, *Astron. J.*, 132, 866
- Ricker, G. R., Winn, J. N., Vanderspek, R., et al. 2014, *J. Astron. Telesc. Instruments, Syst.*, 1, 014003
- Riedel, A. R., Blunt, S. C., Lambrides, E. L., et al. 2017, *Astron. J.*, 153, 95
- Schmitt, J. H. M. M., Fleming, T. A., & Giampapa, M. S. 1995, *ApJ*, 450, 392
- Schneider, A. C., Shkolnik, E. L., Allers, K. N., et al. 2019, *Astron. J.*, 157, 234
- Shaya, E. J. & Olling, R. P. 2011, *Astrophys. J. Suppl. Ser.*, 192, 2
- Shkolnik, E. L., Allers, K. N., Kraus, A. L., Liu, M. C., & Flagg, L. 2017, *Astron. J.*, 154, 69
- Siverd, R. J., Brown, T., Henderson, T., et al. 2018, in *Ground-based Airborne Instrum. Astron. VII*, ed. H. Takami, C. J. Evans, & L. Simard No. July 2018 (SPIE), 231
- Skrutskie, M. F., Cutri, R. M., Stiening, R., et al. 2006, *Astron. J.*, 131, 1163
- Smareglia, R., Bignamini, A., Knapic, C., Molinaro, M., & Collaboration, G. 2014, in *Astron. Data Anal. Softw. Syst. XXIII*, 435
- Soderblom, D. R. 2010, *Annu. Rev. Astron. Astrophys.*, 48, 581
- Somers, G., Cao, L., & Pinsonneault, M. H. 2020, *ApJ*, 891, 29
- Somers, G. & Pinsonneault, M. H. 2015, *ApJ*, 807, 174
- Southworth, J. 2015in , 164–165
- Sperauskas, J., Deveikis, V., & Tokovinin, A. 2019, *A&A*, 31, 1
- Stauffer, J. R., Schultz, G., & Kirkpatrick, J. D. 1998, *ApJ*, 499, L199
- Tody, D. 1986, 733
- Tokovinin, A. 2018, *Astrophys. J. Suppl. Ser.*, 235, 6
- Torres, C. A. O., Quast, G. R., da Silva, L., et al. 2006, *A&A*, 460, 695
- Torres, C. A. O., Quast, G. R., Melo, C. H. F., & Sterzik, M. F. 2008, in *Handb. Star Form. Reg. Vol. II*, ed. B. Reipurth, Vol. 5, 757
- Torres, G., Andersen, J., & Giménez, A. 2010, *Astron. Astrophys. Rev.*, 18, 67
- van Leeuwen, F. 2007, *A&A*, 474, 653
- Voges, W., Aschenbach, B., Boller, T., et al. 1999, *ApJ*, 349, 389
- Weinberg, M. D., Shapiro, S. L., & Wasserman, I. 1987, *ApJ*, 312, 367
- Woolley, R., Epps, E. A., Penston, M. J., & Pocock, S. B. 1970, *R. Obs. Ann.*, 5, 227
- Wright, J. T. & Eastman, J. D. 2014, *Publ. Astron. Soc. Pacific*, 126, 838
- Zacharias, N., Finch, C. T., Girard, T. M., et al. 2013, *Astron. J.*, 145 [arXiv: 1212.6182]
- Zapatero Osorio, M. R., Martín, E. L., Béjar, V. J. S., et al. 2007, *ApJ*, 666, 1205
- Zechmeister, M. & Kürster, M. 2009, *A&A*, 496, 577
- Zucker, S. & Mazeh, T. 1994, *ApJ*, 420, 806
- Zucker, S., Mazeh, T., Santos, N. C., Udry, S., & Mayor, M. 2004, *A&A*, 426, 695
- Zuckerman, B. & Song, I. 2004, *Annu. Rev. Astron. Astrophys.*, 42, 885
- Zuckerman, B., Song, I., Bessell, M. S., & Webb, R. A. 2001, *ApJ*, 562, L87
- Zúñiga-Fernández, S., Bayo, A., Elliott, P., et al. 2021, *A&A*, 645, A30

Table 10. Rotation period derived from the TESS light curves of the LA members compiled from Montes et al. (2001).

<i>Gaia</i> eDR3 ID	α (J2000)	δ (J2000)	P_{rot} [d]
4905600633472735232	00:05:28.45	-61:13:33.06	13.50
4995853014646190080	00:05:52.55	-41:45:11.04	2.95
2860924621205256704	00:06:36.78	+29:01:17.41	6.30
2860839993168688128	00:18:20.90	+30:57:22.03	1.77
4901229043960054784	00:18:26.12	-63:28:38.97	2.30
4901926409210454016	00:24:08.98	-62:11:04.41	1.75
4902014095262270464	00:25:14.66	-61:30:48.33	1.75
532870034006715264	01:02:57.22	+69:13:37.41	12.00
5038817840251308032	01:33:15.81	-24:10:40.67	17.50
2477815222028038144	01:37:35.47	-06:45:37.52	7.50
2498460442625153024	02:41:14.00	-00:41:44.36	1.77
5160075762132997120	02:52:32.13	-12:46:10.97	6.95
5166951386298775552	03:09:42.29	-09:34:46.59	5.52
248004472671281664	03:33:13.49	+46:15:26.54	3.17
3256786534197166080	04:02:36.74	-00:16:08.13	1.50
493935296471302784	04:09:35.04	+69:32:29.01	...
2972231722338351104	05:34:09.16	-15:17:03.18	2.02
4795598309045006336	05:36:56.85	-47:57:52.87	4.60
263916708025623680	05:41:20.34	+53:28:51.81	5.53
3116883781327752704	06:19:08.06	-03:26:20.38	1.36
5266270443442455552	06:18:28.21	-72:02:41.43	2.67
3135225421986580992	07:39:23.04	+02:11:01.18	...
902175202130168064	08:08:56.39	+32:49:11.41	3.38
3097747606079523840	08:07:09.09	+07:23:00.13	22.50
3090083696499828736	08:22:49.95	+01:51:33.55	3.35
718976395775952256	09:03:27.09	+37:50:27.52	2.84
646255212109355136	09:32:43.76	+26:59:18.71	5.43
799093375686189568	09:36:04.28	+37:33:10.36	...
804739952015901056	10:22:10.56	+41:13:46.31	...
3855208897392951808	10:28:55.55	+00:50:27.58	...
5455707157211785216	10:43:28.27	-29:03:51.43	6.90
3789271459953459200	11:04:41.47	-04:13:15.91	6.06
761919883981626752	11:12:32.35	+35:48:50.69	7.40
3585636855608873984	11:47:03.84	-11:49:26.63	...
3901957795343984640	12:25:58.58	+08:03:44.03	...
3520585968137789440	12:29:50.91	-16:31:14.99	...
4010554050558613504	12:32:27.43	+28:05:04.62	...
1717627794711189760	12:37:19.23	+79:12:55.71	7.35
3957887649746831360	12:48:47.05	+24:50:24.81	...
1472718211053416448	13:19:40.13	+33:20:47.52	...
1565867461768654336	13:25:45.53	+56:58:13.77	7.99
1484502295643717888	14:21:08.86	+37:24:03.69	7.50
1668690628102524928	14:39:00.22	+64:17:29.84	2.62
5882581895219920896	15:38:57.55	-57:42:27.27	4.28
5989102478619520000	15:41:11.38	-44:39:40.34	0.89
1222932018450870272	15:49:35.65	+26:04:06.21	...
4503423641091792896	17:55:44.89	+18:30:01.37	...
6721432232656219136	18:12:21.39	-43:26:41.43	13.50
2099385000742174720	19:16:22.09	+38:08:01.43	...
6643589352010758144	19:22:58.94	-54:32:16.98	1.52
6794047652729200640	20:45:09.53	-31:20:27.24	4.83
6456232811155783680	20:57:22.44	-59:04:33.46	10.08
6409848126430575616	21:44:30.12	-60:58:38.88	4.49
2224502448957645312	21:45:52.64	+70:20:53.03	8.12
6564091190988411904	21:48:15.75	-47:18:13.01	...
6410766630956403712	21:50:23.79	-58:18:18.18	...
6408937971321777152	21:52:09.72	-62:03:08.50	0.96
1898230241798771968	21:54:45.04	+32:19:42.86	...
1999733272633122304	22:20:07.03	+49:30:11.76	2.53

Table 10. continued.

<i>Gaia</i> eDR3 ID	α (J2000)	δ (J2000)	P_{rot} [d]
6628926642897745920	22:34:41.64	-20:42:29.56	...
2207738916728293888	23:06:04.85	+63:55:34.41	2.83
2282846074981010688	23:19:26.64	+79:00:12.67	2.72
2395031273585836032	23:32:49.40	-16:50:44.30	...
6387058411482256384	23:39:39.49	-69:11:44.88	3.56

Notes. The associated errors for the rotational periods are around 10% of their value.